HHS Public Access

Author manuscript

Cell Rep. Author manuscript; available in PMC 2023 August 21.

Published in final edited form as:

Cell Rep. 2023 July 25; 42(7): 112803. doi:10.1016/j.celrep.2023.112803.

Proximity-dependent recruitment of Polycomb repressive complexes by the lncRNA *Airn*

Aki K. Braceros[1,2,3,4,5], **Megan D. Schertzer**[1,6,14], **Arina Omer**[13], **Jackson B. Trotman**[1,2,3], **Eric S. Davis**[7], **Jill M. Dowen**[3,10,11,12], **Douglas H. Phanstiel**[3,6,7,8,9], **Erez Lieberman Aiden**[13], **J. Mauro Calabrese**[1,2,3,15,*]

[1]Department of Pharmacology, University of North Carolina, Chapel Hill, NC 27599, USA

[2]RNA Discovery Center, University of North Carolina, Chapel Hill, NC 27599, USA

[3]Lineberger Comprehensive Cancer Center, University of North Carolina, Chapel Hill, NC 27599, USA

[4]Curriculum in Biochemistry and Biophysics, University of North Carolina, Chapel Hill, NC 27599, USA

[5]Curriculum in Mechanistic, Interdisciplinary Studies of Biological Systems, University of North Carolina, Chapel Hill, NC 27599, USA

[6]Curriculum in Genetics and Molecular Biology, University of North Carolina, Chapel Hill, NC 27599, USA

[7]Curriculum in Bioinformatics and Computational Biology, University of North Carolina, Chapel Hill, NC 27599, USA

[8]Department of Cell Biology and Physiology, University of North Carolina, Chapel Hill, NC 27599, USA

[9]Thurston Arthritis Research Center, University of North Carolina, Chapel Hill, NC 27599, USA

[10]Department of Biochemistry and Biophysics, University of North Carolina, Chapel Hill, NC 27599, USA

[11]Department of Biology, University of North Carolina, Chapel Hill, NC 27599, USA

[12]Integrative Program for Biological and Genome Sciences, University of North Carolina, Chapel Hill, NC 27599, USA

[*]Correspondence: jmcalabr@med.unc.edu.

AUTHOR CONTRIBUTIONS

A.K.B. and J.M.C. conceived the study; A.K.B., M.D.S., A.O., J.B.T., and J.M.C. performed the experiments; A.K.B., M.D.S., E.S.D., and J.M.C. performed the analyses; J.M.D., D.H.P., and E.L.A. provided reagents and advice; and A.K.B. and J.M.C. wrote the paper with feedback from the co-authors.

DECLARATION OF INTERESTS

The authors declare no competing interests.

SUPPLEMENTAL INFORMATION

Supplemental information can be found online at https://doi.org/10.1016/j.celrep.2023.112803.

[13]Center for Genome Architecture, Department of Molecular and Human Genetics, Baylor College of Medicine, Houston, TX 77030, USA

[14]Present address: New York Genome Center, New York, NY 10013, USA

[15]Lead contact

SUMMARY

During mouse embryogenesis, expression of the long non-coding RNA (lncRNA) *Airn* leads to gene repression and recruitment of Polycomb repressive complexes (PRCs) to varying extents over a 15-Mb domain. The mechanisms remain unclear. Using high-resolution approaches, we show in mouse trophoblast stem cells that *Airn* expression induces long-range changes to chromatin architecture that coincide with PRC-directed modifications and center around CpG island promoters that contact the *Airn* locus even in the absence of *Airn* expression. Intensity of contact between the *Airn* lncRNA and chromatin correlated with underlying intensity of PRC recruitment and PRC-directed modifications. Deletion of CpG islands that contact the *Airn* locus altered long-distance repression and PRC activity in a manner that correlated with changes in chromatin architecture. Our data imply that the extent to which *Airn* expression recruits PRCs to chromatin is controlled by DNA regulatory elements that modulate proximity of the *Airn* lncRNA product to its target DNA.

In brief

Braceros et al. map interactions between DNA regulatory elements, Polycomb repressive complexes (PRCs), and the lncRNA *Airn*. They find that the presence of *Airn* lncRNA and PRCs correlates in lock-step on chromatin and that specific DNA regulatory elements modulate intensity of repression by *Airn* in different ways.

Graphical abstract

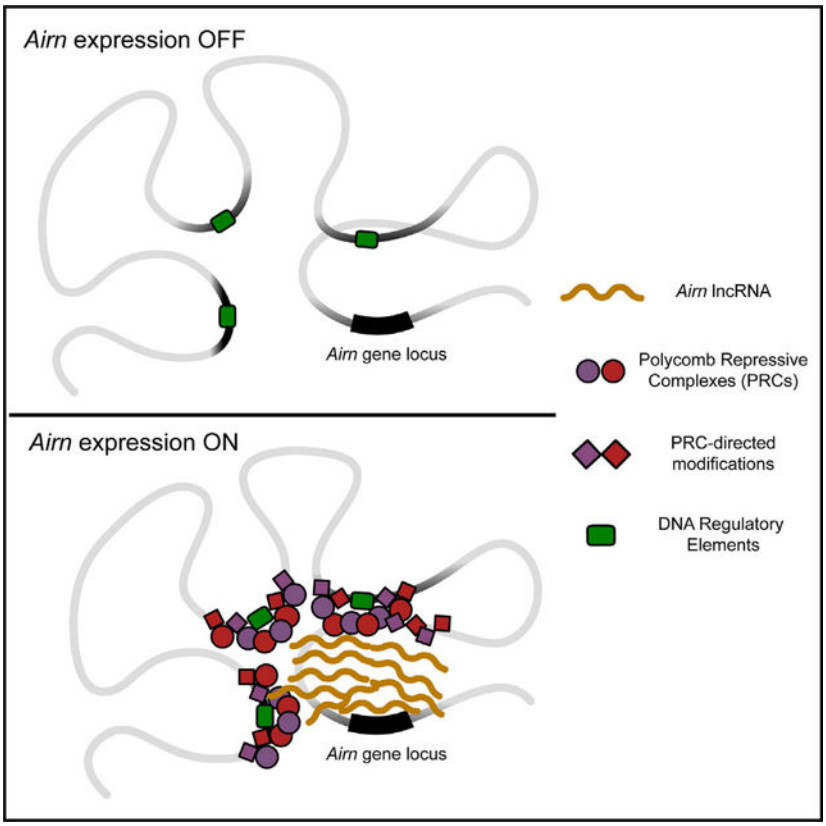

INTRODUCTION

Genomic imprinting is a process known to occur for some ~150 mammalian genes, resulting in their preferential expression from one parentally inherited allele over the other. Dysregulated imprinting can lead to developmental disorders, cancer, and changes in metabolism. Studies of genomic imprinting have also yielded important insights into fundamental mechanisms of gene regulation, including the recognition that long non-coding RNAs (lncRNAs) control the expression of genes that are essential for proper human development.[1–4]

Airn (*Antisense of Igf2r Non-Protein Coding RNA*) is a gene that in mice is imprinted and produces a lncRNA specifically from the paternal allele of chromosome (chr) 17. The *Airn* locus produces lncRNA transcripts that are upward of ~90 kb in length but have heterogeneous 3′ ends.[5] In addition, *Airn* transcripts are lowly abundant, short-lived, retained near their site of transcription, predominantly unspliced, and not obviously conserved outside of rodents.[6–12] Nevertheless, *Airn* expression results in transcriptional repression over a domain that spans ~15 Mb in extraembryonic tissues of the mouse, the largest autosomal region known to be under the control of a repressive lncRNA.[13,14] Repression by *Airn* occurs predominantly, if not exclusively, in *cis*, on the same chromosome from which the lncRNA is transcribed.[13,14]

The mechanism by which *Airn* mediates repression over its 15-Mb target domain is not clear. *Airn*'s lack of conservation, lack of splicing, and the instability and variable length of its RNA product have raised questions about whether it is the *Airn* lncRNA itself or merely the act of its transcription that mediates repression.[15,16] Accumulating data are supportive of a role for the *Airn* lncRNA product in mediating long-range repression,[14,17,18] yet it remains unclear what properties of the RNA may enable it to do so. Moreover, the intensity of repression across the *Airn* target domain is non-uniform,[14] implying that features of the genome influence repression by *Airn* in ways that are not yet clear.

For its full repressive effect, *Airn* requires several histone-modifying enzymes, including the Polycomb repressive complexes (PRCs), which are known to be recruited to chromatin by the expression of a handful of other lncRNAs, including *Xist*.[19–21] There are two major PRCs, PRC1 and PRC2, each of which can be classified into different sub-complexes that contain core and auxiliary components.[22] PRC1 monoubiquitinates histone H2A at lysine 119 (H2AK119ub) and is composed of canonical and variant complexes termed cPRC1 and vPRC1, respectively. PRC2 tri-methylates histone H3 at lysine 27 (H3K27me3) and is composed of sub-complexes called PRC2.1 and PRC2.2. The different auxiliary factors that distinguish PRC sub-complexes modulate their enzymatic activities, interaction partners, effects on three-dimensional (3D) genome organization, and ultimately, effects on gene expression.[22] For example, specific forms of vPRC1 have been shown to interface the most closely with the lncRNA *Xist*.[23,24]

We previously found that in mouse trophoblast stem cells (TSCs), expression of *Airn* represses genes and induces the deposition of H2AK119ub and H3K27me3 in a highly non-uniform fashion across a 15-Mb target domain.[14] Intensity of gene repression and PRC-directed modifications could be modulated by altering levels of *Airn* transcription from its endogenous promoter, supporting a role for the *Airn* lncRNA product in PRC recruitment and indicating that chromatin within the *Airn* target domain is highly sensitive to levels of *Airn*. Within the domain, the regions most highly decorated in PRC-deposited modifications centered around a subset of CpG island (CGI) promoters bound by the catalytic components of PRC1 and PRC2, even on the maternal allele, which does not express *Airn*. These and other data led us to hypothesize that the non-uniform repression across the *Airn* target domain was mediated by DNA regulatory elements that preferentially contact the *Airn* locus through 3D space and focus *Airn*'s repressive activity over certain genomic regions.

Herein, we set out to test that hypothesis and examine in greater detail the extent to which repression by *Airn* is influenced by chromatin architecture and underlying features of the genome. In TSCs and mouse embryonic stem cells (ESCs), we found that variation in repression across the domain could be partly explained by 3D DNA contacts that exist in the absence of *Airn* expression, which appear to bring certain genomic regions in closer proximity to the *Airn* locus over others. Regions within the domain that associated the most robustly with the *Airn* lncRNA product associated the most robustly with PRC1 and PRC2. Seemingly similar DNA regulatory elements located in different regions within the target domain had different effects on *Airn*-dependent repression, possibly by modulating local PRC recruitment or frequency of contact between *Airn* and target DNA. Our data support the notion that the *Airn* lncRNA product recruits several forms of PRC1 and PRC2 to

chromatin and demonstrates that DNA regulatory elements can control the regional intensity with which it does so.

RESULTS

Airn expression induces large-scale changes to chromatin architecture

Because *Airn* is monoallelically expressed and *cis* acting, its target domain exists in different states on each allele; the paternal allele being repressed by *Airn*, and the maternal allele existing in the non-repressed state. For this reason, we and others have studied *Airn* in F1-hybrid cell lines or animals derived from different strains of inbred mice.[13,14,17] In F1-hybrids, physical events associated with maternal and paternal alleles can be distinguished by single-nucleotide polymorphisms (SNPs) in sequencing reads.[25]

To determine how *Airn* expression alters chromatin architecture, we performed *in situ* Hi-C[26] in three F1-hybrid TSC lines: one line derived from a cross between a CAST/EiJ mother and C57BL/6J father (C/B TSCs), one derived from the reciprocal cross, a C57BL/6J mother and CAST/EiJ father (B/C TSCs), and a third TSC line in which we previously used CRISPR to insert a triple-polyadenylation cassette ~3 kb downstream of the *Airn* transcription start site in C/B TSCs, generating a mutant with an expected null phenotype (C/B *Airn* truncation TSCs[8,14]). Hi-C libraries were generated in biological triplicate from each TSC line and sequenced to an aggregate depth per genotype of at least 1.6 billion paired-end 150-nt reads (Table S1).

We constructed allele-specific contact maps to examine how *Airn* expression alters chromatin architecture across its target domain.[27,28] In C/B wild-type TSCs, on the paternal B6 allele, which expresses *Airn*, relative to the maternal CAST allele, which does not, we observed a reduction in short-range DNA contacts concomitant with an increase in long-range contacts, which were largely contained within the 15-Mb target domain previously shown to be repressed by *Airn* in TSCs (Figures 1Ai and 1Bi[14]). The greatest increases in contact occurred within a 4.5-Mb interval that extended from the *Airn* locus and terminated at the genes *Prr18*, *T*, and *Pde10a* (Figures 1Ai and 1Bi). In *Airn* truncation TSCs, the increased contacts were not detectable, demonstrating their dependence on *Airn* expression (Figures 1Aii and 1Bii). Moreover, the overall trends that were observed in C/B wild-type TSCs were also observed in the reciprocal F1-hybrid cell line, B/C wild-type TSCs, in which the paternal, *Airn*-expressing allele is of CAST origin, confirming that differences in chromatin architecture between paternal and maternal alleles are due to parent-of-origin and not strain-specific effects (Figures 1Aiii and 1Biii). The regions that underwent the strongest *Airn*-dependent changes in contact frequency were the ones that most clearly shifted from the “A” to the “B” chromosome compartment specifically on the alleles that expressed *Airn* (Figure 1Ci–iii; Figure S1[,26,29]). Thus, in TSCs, *Airn* expression induces large-scale changes to chromatin architecture that are largely contained within a 15-Mb genomic interval previously shown to be subject to *Airn*-dependent repression.[13,14]

Airn-dependent changes in chromatin architecture coincide with the presence of PRC-deposited modifications

To understand how DNA contacts with the *Airn* locus correlate with *Airn*-dependent repression, we created a series of "viewpoint" plots, in which contacts between *Airn* and surrounding regions were extracted and visualized in two dimensions. Consistent with the heatmaps of Figure 1, we observed a dramatic increase in *Airn*-dependent contacts with the *Airn* locus on the paternal allele toward the centromeric end of chr17, including a pronounced shoulder of increased contacts surrounding the genes *Prr18*, *T*, and *Pde10a* (Figure 2A). We also observed augmented contacts between *Airn* and the gene *Qk* on both alleles in all TSC lines profiled (Figure 2A). In C/B wild-type TSCs, the intensity of allele-specific contacts with *Airn* as measured by Hi-C correlated remarkably well with allele-specific distances to the *Airn* locus that we had previously measured by DNA fluorescence *in situ* hybridization (FISH), corroborating both forms of measurement (Figure 2B; Spearman's r of −0.82 and −0.95 and p = 0.007 and 0.001 on maternal and paternal alleles, respectively; FISH probe locations from Schertzer et al.[14] shown in Figure 2Ai).

The magnitude of *Airn*-dependent contacts (i.e., paternal contacts subtracted from maternal contacts) also correlated well with the underlying intensity of *Airn*-dependent, PRC-directed chromatin modifications (Figures 2C–2F; Spearman's r between *Airn*-dependent contacts and H3K27me3 and H2AK119ub in C/B TSCs, 0.69 and 0.67, respectively, $p < 2e{-}16$ for both comparisons). Moreover, we used chromatin immunoprecipitation sequencing (ChIP-seq) to profile seven individual components of PRC1 and PRC2 (RING1B, RYBP, CBX7, KDM2B, EZH2, MTF2, and JARID2). Within the target domain, six out of seven PRC components exhibited a signature of *Airn*-responsiveness, defined as a broad shoulder of paternal enrichment on the centromeric side of the *Airn* locus (Figure S2A). The same six PRC components appeared responsive to *Xist* (Figure S3). The sole exception was the PRC1.1 component KDM2B (Figures S2A and S3). Because the PRCs and their modifications to chromatin can induce DNA compaction,[7,22,26] and *Airn* expression correlates with the presence of PRCs within its target domain, our data are consistent with the notion that the large-scale changes in genome architecture induced by expression of *Airn* depend, at least in part, on the PRCs and their modifications to chromatin.

Airn-dependent repression centers around regions that form pre-existing contacts with the *Airn* locus and harbor CGIs bound by vPRC1

DNA contacts detected by Hi-C can occur by chance with a frequency that increases with decreasing distance from the locus in question.[26] To quantify the relative intensity of contacts that occur with the *Airn* locus after correcting for distance-dependent effects, we created a series of observed-over-expected (O/E) plots with *Airn* as the viewpoint, in which detected contacts were normalized by those expected from a distance-dependent decay model.[26]

These O/E viewpoint plots revealed three local maxima of contact with *Airn* that fell within the 4.5-Mb genomic interval most intensely repressed by *Airn*, extending from the *Airn* locus and terminating at *Prr18*, *T*, and *Pde10a* (Figures 2, 3A, and S4). Specifically, maxima were detected surrounding the genes *Prr18*/*T*/*Pde10a*, the gene *Qk*, and the gene *Slc22a3*

(Figures 3A and S4). Although intensity of O/E contact with *Prr18/T/Pde10a* increased dramatically upon expression of *Airn*, intensity of O/E contact with *Qk* and *Slc22a3* changed to lesser extents or not at all (Figures 3A and S4). All three maxima were present in *Airn* truncation TSCs, highlighting contact with the *Airn* locus even in the absence of *Airn* expression (Figures 3Aii and S4). Each gene within these maxima is driven by CGI promoters that we found in previous work to either bind high levels of RING1B and EZH2 (in the cases of *Prr18/T/Pde10a* and *Qk*) or be present in the region of the *Airn* target domain that accumulates the highest levels of *Airn*-dependent, PRC-directed chromatin modifications (in the case of *Slc22a3*) (Figure 2).[14]

We were intrigued that points of contact with *Airn* centered around PRC-bound CGIs. CGIs often mark high-density sites of PRC binding, and PRCs and the modifications that they deposit on chromatin can mediate long-range 3D contacts independently of CTCF and Cohesin.[30–39] Moreover, the genes within the points of contact–*Pde10a*, *Qk*, and *Slc22a3*–are all repressed by *Airn* in TSCs[14] (Table S2). Also, the *Airn* gene body itself harbors two CGIs that bind RING1B/PRC1,[14] and the *Airn* lncRNA has previously been found to associate with the *Slc22a3* CGI.[18] Lastly, although the reasons remain unclear, we previously found that deletion of the *Slc22a3* CGI resulted in a dramatic loss of *Airn*-induced accumulation of H3K27me3, most notably in the 4.5-Mb interval beginning at *Airn* and terminating at *Prr18*, *T*, and *Pde10a*.[14] These data raise the possibility that features associated with the CGIs in regions that form augmented DNA contacts with the *Airn* locus play roles in modulating the local intensity of *Airn*-dependent repression.

With that possibility in mind, we used ChIP-seq to examine what factors and chromatin modifications were enriched over CGIs contained within points of 3D contact with *Airn*. These included CGIs at *Pde10a*, *Qk*, *Slc22a3*, and *Airn* itself, as well as the CGI promoter of the gene *Map3k4*. Like *Qk*, *Map3k4* is repressed by *Airn* and forms a detectable contact with the *Airn* locus by Hi-C (Figures 3A and S4B) but partially escapes silencing and sits within a region that resists the local accumulation of *Airn*-induced, PRC-deposited chromatin modifications (Figures 2C and 2D; Table S2). In total, we examined ChIP-seq data for the same seven PRC components whose allelic tiling density profiles are shown in Figures S2 and S3, four chromatin modifications (H3K27me3, H2K119ub, H3K4me2, and H3K27ac), and two architectural factors (SMC1A/Cohesin and CTCF; data from this study, Schertzer et al.,[14] and Calabrese et al.[40]). A summary of the allele-specific enrichment of each factor is found in Table S3, and the total, non-allelic genome browser density tracks are shown in Figure 3B. The asterisks above each CGI indicate whether the factor was detected on the maternal allele, paternal allele, or both (Figure 3B; Table S3).

Although there was not one singular pattern of enrichment, notable similarities emerged. Each CGI except for the one found at the promoter of *Airn* showed some level of peak-like enrichment for vPRC1 on the maternal allele (Figure 3B). Likewise, all of the CGIs examined except for the one at the *Airn* promoter showed peak-like enrichment of at least one of the two chromatin modifications associated with transcriptional activation (H3K4me2 or H3K27ac), also on the maternal allele. SMC1A/Cohesin was also detected on the maternal allele of these same sets of CGIs, although its intensity of enrichment was low relative to intergenic peaks (Figure 3B). Thus, the regions within the target domain that form

3D contacts with the *Airn* locus on the maternal allele all harbor CGI promoters that are enriched in vPRC1, Cohesin, and signatures of transcriptional activity.

In contrast, CGIs in the region that underwent the strongest *Airn*-dependent changes in chromatin architecture, surrounding the genes *Prr18*, *T*, and *Pde10a*, were associated with sharp peaks of cPRC1 and PRC2, as well as vPRC1 (Figures 3B and S2A). Of those CGIs, the CGI at *Pde10a* was associated with the highest levels of both PRC1 and PRC2 (Table S3). Likewise, the intergenic regions that underwent the strongest *Airn*-dependent changes in chromatin architecture were similarly enriched in cPRC1 and PRC2, as well as vPRC1 (Figure S2A). Thus, although the presence of vPRC1, Cohesin, and transcription can identify regions that contact the *Airn* locus in the absence of *Airn* expression, the presence of cPRC1 and PRC2 at both CGIs and intergenic regions correlate more strongly with the presence of *Airn*-dependent, PRC-deposited modifications and long-range changes to architecture.

Presence of *Airn* lncRNA on chromatin correlates with the presence of PRC1 and PRC2 and centers around pre-existing contacts with the *Airn* locus

We next sought to determine whether the *Airn* lncRNA itself was preferentially associated with specific DNA regions. To address this question, we used CHART-seq, an approach to identify genomic regions located proximal to lncRNAs.[41] We performed CHART-seq for *Airn* (Figure S5A) in C/B wild-type TSCs, in *Airn* truncation TSCs, and in a C/B TSC line from Schertzer et al.,[14] in which we used CRISPR-Cas9 to over-express *Airn* from its endogenous promoter (*Airn* highly expressing [H-E] TSCs). qRT-PCR confirmed expected levels of *Airn* expression in each TSC line (Figure S5B).

In C/B wild-type TSCs, *Airn* CHART-seq revealed enrichment of DNA on the paternal, but not maternal, allele across the *Airn* target domain, beginning near the centromere and ending ~3 Mb downstream of the *Airn* locus, the same region where the last *Airn*-induced PRC-dependent modifications are visible (Figures 4Ai, 4Bi, S5C, and S5D). In H-E TSCs, the enrichment increased with over-expression of *Airn* (Figures 4Aii, S5C, and S5D). Conversely, in *Airn* truncation cells, DNA enrichment from the paternal allele was lost (Figures 4Aiii, S5C, and S5D). These data indicate that DNA recovered by CHART is sensitive to overall levels of *Airn* expression. Moreover, we observed a strong correlation between paternal *Airn* CHART-seq and H3K27me3, RING1B, and EZH2 ChIP-seq signal throughout the target domain (lowest Spearman's r across C/B wild-type and H-E TSC comparisons is 0.53, $p < 2e{-}9$ for all comparisons; Figures 4A–4D). Calibrated and non-calibrated ChIP-seq for H3K27me3 and EZH2 showed the same patterns of enrichment (Figures 4B and 4D vs. S2B and S2C). We were especially struck by the lower CHART-seq signal in H-E TSCs that began just upstream of *Map3k4* and *Qk*, genes that are repressed by *Airn* but located at inflection points where the intensity of PRCs and PRC-directed modifications drops precipitously (Figures 4A–4D). Likewise, particularly in H-E TSCs, local maxima of *Airn* lncRNA association coincide with genomic regions that form local maxima of Hi-C O/E contacts with the *Airn* locus even in the absence of *Airn* expression (Figures 4A and 3Aii).

We also performed *Airn* CHART-seq in mouse ESCs, in which we used CRISPR-Cas9 to force expression of *Airn* from its endogenous promoter (H-E ESCs). In H-E ESCs, *Airn* was expressed at a level approximately equal to wild-type TSCs (Figure S5B). As a negative control, we performed CHART-seq in uninduced ESCs, which do not express meaningful levels of *Airn*. We also performed ChIP-seq to determine the extent to which DNA retrieved by CHART correlated with intensity of H3K27me3. We observed associations between the *Airn* lncRNA and DNA in H-E ESCs across a domain that was remarkably similar in size and contour to the domain associated with *Airn* in TSCs (Figure 4F vs. 4A). Also, as in TSCs, *Airn* associations were significantly correlated with underlying H3K27me3 (Figure 4F vs. 4G; Spearman's r = 0.64, p = 7.9e–14), and *Map3k4* and *Qk* resisted *Airn* and PRC-directed modifications in H-E ESCs (Figures 4E and 4F). Furthermore, we observed that local maxima of Hi-C O/E contacts with the *Airn* locus in ESCs coincided or were proximal to local maxima of *Airn* lncRNA association and H3K27me3, most notably at *Prr18*|*T*|*Pde10a*, *Slc22a3*, and on the telomeric side of *Airn*, in a region surrounding the genes *Dact2* and *Wdr27* (Hi-C;[42] Figure 4G vs. 4E and 4F). The only exception to this pattern was at *Qk*, which despite forming DNA contacts with the *Airn* locus, resisted contacting the *Airn* lncRNA and accumulating PRC-directed modifications in both TSCs and ESCs.

Altogether, our data support the notion that a major function of the *Airn* lncRNA product is to recruit the PRCs to chromatin over a 15-Mb domain, and that proximity to the *Airn* lncRNA product dictates the intensity with which the recruitment occurs. Moreover, pre-existing DNA contacts, those that occur with the *Airn* locus in the absence of *Airn* expression, center within regions of chromatin that become decorated in PRC-directed modifications upon *Airn* expression. Lastly, *Map3k4* and *Qk* resist associations with the *Airn* lncRNA despite forming DNA contacts with the *Airn* locus.

DNA regulatory element deletions alter levels of PRC-directed modifications and gene repression throughout the *Airn* target domain

Our data indicate that regional proximity to the *Airn* lncRNA product correlates with local intensity of gene repression and PRC recruitment. To study the extent to which DNA regulatory elements might control proximity to *Airn*, we focused on the region surrounding the genes *Prr18*|*T*|*Pde10a*, which harbors several CGIs that bind PRCs and undergoes increased frequency of 3D contact with the *Airn* locus upon *Airn* expression (Figures 2 and 3). We used CRISPR-Cas9 to individually delete the CGI promoters of *T* and *Pde10a*, as well as a 190-kb cluster of intergenic CTCF and SMC1A/Cohesin peaks located between *T* and *Pde10a* (pink rectangles in Figures 3B and S6A–S6C). We derived heterozygous clonal TSC lines harboring deletions for each element on their paternal alleles (Δ*T*, four lines; Δ*Pde10a*, two lines; Δ*Cluster*, two lines; Figures S5A–S5C). As controls, we derived four clonal non-targeting (NTG) TSC lines that harbor the same doxycycline-inducible *Cas9* transgene and underwent the same process of electroporation, clonal selection, and induction as above, but that express a NTG sgRNA that does not match the mouse genome (Figures S6A–S6D; Table S5). In addition, we revived the two TSC lines in which we previously deleted the *Slc22a3* CGI on the paternal allele (Δ*Slc22a3* TSCs from Schertzer etal.[14]; Figure S6D). In that study, we found that *Slc22a3* CGI deletion caused a ~4.5-Mb reduction

in the intensity of H3K27me3, beginning essentially at the *Slc22a3* gene and extending through the distal cluster of PRC-bound CGIs at *Prr18*/*T*/*Pde10a*.[14] qRT-PCR and RNA sequencing (RNA-seq) showed that *Airn* expression levels varied by no more than 2-fold across our panel of lines (Figure S6E).

We performed H3K27me3 and H2AK119ub ChIP-seq, as well as RNA-seq, to examine how the deletions affected PRC activity and gene repression. Relative to NTG controls, ChIP-seq in Δ*Slc22a3* TSCs revealed a dramatic loss of H3K27me3 and H2AK119ub throughout the *Airn* target domain (Figure 5A vs. S6F and S6G), consistent with and extending results from Schertzer et al.[14] However, whereas deletion of the *T* CGI had little to no effect, deletion of the *Pde10a* CGI unexpectedly caused a dramatic increase in the levels of H3K27me3 and H2AK119ub throughout the target domain, opposite to that observed in Δ*Slc22a3* TSCs (Figures 5B, 5C, and S6G). Deletion of the cluster of CTCF and SMC1A/Cohesin peaks similarly increased H3K27me3 and H2AK119ub (Figure 5D). Cross-genotype comparisons within the target domain and across the remainder of chr17 are shown in Figure S6G.

RNA-seq from deletion clones showed changes in gene expression consistent with changes in PRC-deposited modifications (Figure 5E vs. 5A–5D). In our previous study, we identified 27 genes within the target domain that were subject to repression by *Airn*.[14] In Δ*Slc22a3* TSCs, the relative paternal expression of these 27 genes increased significantly compared with their baseline in NTG, up to an average level that was slightly less than that observed in *Airn* truncation TSCs, which are effectively null mutants[14] (NTG vs. Δ*Slc22a3* [A12 and A13 clones], $p = 0.038$ and 0.025, respectively, Welch two-sample t test; Figure 5E). Conversely, in Δ*Pde10a* and Δ*Cluster* TSCs, paternal expression of these genes decreased relative to NTG TSCs, albeit with variability between clones (NTG vs. Δ*Pde10a* and NTG vs. Δ*Cluster*; Figure 5E). The decreased expression in Δ*Pde10a* and Δ*Cluster* TSCs was not as strong as that observed in *Airn* H-E TSCs (Figure 5E) but was nevertheless consistent with the increase in PRC-deposited modifications (Figures 5C and 5D).[14] Thus, seemingly similar DNA regulatory elements play critical but different roles in dictating the regional intensity of gene repression and PRC recruitment induced by *Airn* within its 15-Mb target domain.

Changes in DNA contacts with *Airn* mirror changes in PRC activity caused by regulatory element deletion

To gain insight into the effects caused by regulatory element deletion, we used *in situ* Hi-C to examine DNA contacts in NTG, Δ*Slc22a3*, and Δ*Pde10a* TSCs (Table S1). Consistent with changes in gene repression and PRC-deposited modifications, deletion of the *Slc22a3* and *Pde10a* CGIs alternately diminished and increased *Airn*-dependent contacts across the entire target domain, coincident with corresponding changes in the intensities of compartmentalization (Figures 6A, 6B, and S7).

Examining contacts from the *Airn* viewpoint provided additional insights (Figures 6C and 6D). Deletion of the *Slc22a3* CGI was coincident with reduced levels of *Airn*-dependent contacts throughout the domain, with a possible exception at *Qk* (Figures 6Cii and 6Dii). Proportionally, the greatest decreases in *Airn*-dependent contacts surrounded *Prr18*/*T*/*Pde10a* (Figures 6Cii and 6Dii). In contrast, in Δ*Pde10a* cells, *Airn*-dependent contacts

increased uniformly except at *Prr18/T/Pde10a* (Figures 6Ciii and 6Diii). Thus, deletion of the *Slc22a3* CGI reduced the interaction between *Airn* and DNA throughout its target domain, whereas deletion of the *Pde10a* CGI increased the interaction between *Airn* and all other regions in the domain save *Prr18/T/Pde10a*.

Airn expression is coincident with dissolution of DNA loops encasing *Slc22a3* and a local increase in PRC-directed modifications

We next examined our data to determine how deletion of the *Slc22a3* CGI might restrict repression by *Airn*. In our major Hi-C datasets (described in Figure 1), we noted that the *Slc22a3* and *Airn* genes are located within the same contact domain (a contiguous region exhibiting high levels of inter-locus interactions), where they sit within nested DNA loops anchored by CTCF and Cohesin (Figures 7A and 7B). By Hi-C, the loops that surround *Slc22a3* were reduced by *Airn* expression, to the extent that they are no longer detectable by the significant interaction peak (SIP) algorithm on *Airn*-expressing alleles (Figure 7A).[43] Likewise, we observed a relative reduction in SMC1A and CTCF binding at those same loop anchors, again on *Airn*-expressing alleles, consistent with the reduced loop intensity (Figure 7B). We also searched for these DNA loops in NTG, Δ*Slc22a3*, and Δ*Pde10a* Hi-C data, but lower sequencing depth (~600 million read pairs per genotype) precluded a high-confidence analysis. Nonetheless, visual inspection of loops identified in our high-depth datasets was consistent with the notion that the *Slc22a3* CGI is required for *Airn*-dependent dissolution of the nested loops encasing *Slc22a3* (Figure 7C, note relative increase in intensity at loop anchor regions in the Δ*Slc22a3* genotype, denoted by the two gray arrows). We also observed that deletion of the *Slc22a3* CGI led to a local drop in H3K27me3 and had a lesser yet significant effect on H2AK119ub (Figure 7D). Thus, in contrast with the *Pde10a* CGI, which may effectively restrict surrounding regions from contacting *Airn* through mechanisms that remain to be determined, it is conceivable that prior to *Airn* expression, nested loops that encase *Slc22a3* and *Airn* may reduce the latter's ability to interact with distal DNA. Upon *Airn* expression, recruitment of PRCs locally, promoted by the *Slc22a3* CGI, could antagonize Cohesin[37–39] and disrupt loops that then enable *Airn* to contact distal regions of chromatin more efficiently.

DISCUSSION

We report a series of intriguing relationships between 3D DNA contacts, DNA regulatory elements, and PRC recruitment within the largest autosomal region known to be repressed by a mammalian lncRNA. Our results support the view that *Airn* is a potent *cis*-acting lncRNA that functions to maintain gene repression and recruit the PRCs within a 15-Mb domain on mouse chr17. We show that extent of repression maintained by *Airn* can be modulated by discrete DNA regulatory elements that control the proximity of *Airn* to its genomic targets, a paradigm likely relevant to other domains governed by strong locus control regions, including the inactive X chromosome.

Using *in situ* Hi-C, we observed that expression of *Airn* is accompanied by changes in 3D contacts and compartmentalization on the centromeric side of the *Airn* locus. These changes correlated in step with the intensity of *Airn*-induced H3K27me3 and H2AK119ub

and centered around three regions that contact the *Airn* locus even in the absence of *Airn* expression. Each of these regions harbors CGI promoters that bind components of vPRC1, exhibits signatures of transcriptional activity, and is located proximal to peaks of Cohesin on both the maternal and the paternal alleles. Extent of association with the *Airn* lncRNA, as assessed by CHART-seq, also correlated in step with the intensity of PRCs and PRC-directed modifications and centered around pre-existing DNA contacts, in both TSCs and ESCs. Of the seven different PRC subunits we profiled by ChIP-seq, all except KDM2B were responsive to *Airn*. Two genes, *Map3k4* and *Qk*, resisted accumulating PRC-directed modifications, despite both genes being repressed by *Airn* and forming contacts with the *Airn* locus. Moreover, the intensity of DNA contacts between *Map3k4*, *Qk*, and the *Airn* locus was relatively unchanged by *Airn* expression, and relative to surrounding regions, *Map3k4* and *Qk* resisted association with the *Airn* lncRNA.

Together, our data support the notion that spatial proximity to the *Airn* lncRNA product induces gene repression and, in most cases, also induces the accumulation of multiple forms of PRC1, PRC2, and PRC-directed chromatin modifications. *Airn* is a short-lived RNA that does not diffuse away from its site of transcription.[12,14] Thus, consequently, the regions that are most sensitive to repression by *Airn* are predisposed to contacting the *Airn* locus even in the absence of *Airn* expression. In turn, considering our findings along with prior data showing that the PRCs and their modifications to chromatin can induce DNA compaction,[7,22,26] it seems likely that *Airn*-recruited PRCs and the modifications they deposit on chromatin are responsible for the major changes in chromatin architecture induced by *Airn* expression. Such changes would presumably potentiate *Airn*-dependent repression, stabilizing the process by positive feedback.

Three notable regions within the *Airn* target domain, encompassing the genes *Slc22a3*, *Qk*, and *Prr18/T/Pde10a*, exhibited augmented contacts with the *Airn* locus even in the absence of *Airn* expression. Of these regions, only *Slc22a3* formed a detectable DNA loop anchored at the *Airn* locus.[43] However, each of the regions harbored CGI promoters that themselves were associated with vPRC1, signatures of transcriptional activity, and nearby peaks of Cohesin. Prior works would suggest that any or all of these features could facilitate interactions between the regions and *Airn* DNA.[26,31,44] Upon expression of *Airn*, the region encompassing *Prr18/T/Pde10a* exhibited peak-like increases in contact with the *Airn* locus, whereas the intensity of detectable contacts with *Qk* and *Slc22a3* remained relatively unchanged. Deletion of specific DNA regulatory elements within the *Prr18/T/Pde10a* and *Slc22a3* regions affected the ability of *Airn* to repress genes, induce PRC-directed modifications, and induce changes to chromatin architecture over megabases. Thus, DNA elements shape long-range contacts within the *Airn* target domain in ways that extend beyond single loop-based models of regulation.[44]

Considered together, our data support the view that the extent of repression across the *Airn* target domain is governed by an equilibratory network of DNA regulatory elements that through direct or indirect means controls spatial proximity to the *Airn* lncRNA product (Figure 7E). Shifting the equilibrium in either direction has consequences on gene expression, chromatin modifications, and chromatin architecture. Indeed, we identified one CGI that appears to promote certain long-range contacts while restricting others (*Pde10a*)

and another CGI that may promote long-range contacts by serving as a local Polycomb response element (*Slc22a3*; Figure 7E).[45] To the latter point, a prior study demonstrated that *Airn* DNA preferentially interacts with the *Slc22a3* locus when the *Airn* lncRNA is not expressed,[17] consistent with a model whereby *Airn*-induced, PRC-directed chromatin modifications at *Slc22a3* help to disengage the *Airn* locus from local DNA interactions and promote distal ones. Meanwhile, the CGI promoters of *Map3k4* and *Qk* gave the appearance of serving as boundary elements that attenuate local spread of repression by *Airn*. Our data suggest that variation in the genetic or epigenetic content of a DNA regulatory element has the potential to control gene expression by altering spatial equilibria between genes and locus control regions, be those repressors or enhancers.[46–51] By extension, unrecognized alterations to spatial equilibria that modulate contact with locus control regions may contribute to the challenge of assigning target genes to disease-associated SNPs.[52]

Repression of the *Airn*-target gene *Igf2r* is due to the act of *Airn* transcription and does not depend on the *Airn* lncRNA product.[15] The mechanisms responsible for long-range repression by *Airn* remain unclear. Our observation that *Airn* lncRNA association and PRC-directed chromatin modifications correlate in lock-step over a 15-Mb domain in both TSCs and ESCs, together with data from Schertzer et al.,[14] Andergassen et al.,[17] and Nagano et al.[18] support the idea that *Airn* is a potent *cis*-acting repressive lncRNA that recruits the PRCs and possibly other repressive enzymes to chromatin. Future studies are needed to definitively prove this notion and demonstrate the mechanism by which the *Airn* lncRNA might mediate its longrange repressive effects.

Limitations of the study

Considering that *Airn* acts largely, if not exclusively, in *cis*, F1-hybrid TSCs harbor an internal control in all genomic profiling experiments, in the form of the allele on which *Airn* is not expressed. Throughout our study, we interpret local differences in signal between *Airn*-expressing and non-expressing alleles to reflect *Airn*-dependent effects. Within individual TSC lines, these differences can be interpreted as absolute. However, when comparing signals between different TSC lines, particularly on *Airn*-expressing alleles, our Hi-C, CHART, and almost all ChIPs were performed under conditions that enable us to comment on relative, but not absolute, differences. Also, although the model in Figure 7 provides a parsimonious explanation of our data, our observations regarding 3D DNA contacts are correlative and we have not proven causation. It is also unclear to what extent *Airn* expression may induce changes in chromatin conformation independent of the PRCs. Lastly, the mechanisms by which *Airn* might recruit PRCs to chromatin are unclear. It is also unclear what molecular constituents occupy the interface between the *Airn* lncRNA and its genomic targets. If studies of *Xist* are any guide,[53,54] it is likely that many hundreds of molecules of protein surround each molecule of *Airn*.

STAR★METHODS

RESOURCE AVAILABILITY

Lead contact—Further information and requests for resources and reagents should be directed to and will be fulfilled by the lead contact, Mauro Calabrese (jmcalabr@med.unc.edu).

Materials availability—Plasmids and cell lines generated in this study are available upon request.

Data and code availability

- All raw and processed sequencing data generated in this study have been deposited at GEO and are publicly available as of the date of publication. Accession numbers are listed in the key resources table. All new and published datasets analyzed are summarized in Table S4. Oligonucleotides used are detailed in Table S5.
- All original code has been deposited at Zenodo and Github and is publicly available as of the date of publication. DOIs are listed in the key resources table.
- Any additional information required to reanalyze the data reported in this paper is available from the lead contact upon request.

EXPERIMENTAL MODEL AND STUDY PARTICIPANT DETAILS

TSC culture—The mouse C/B TSC and B/C TSC lines used in this work correspond to the CAST/EiJ maternal/C57BL/6J paternal (C/B) and C57BL/6J maternal/CAST/EiJ paternal (B/C) TSCs used in[40,64] and are referred to as CB.1 and BC.1 TSCs in.[64] TSCs were cultured as in.[65] Briefly, TSCs were cultured on gelatin-coated, pre-plated irradiated mouse embryonic fibroblast (irMEF) feeder cells in TSC media (RPMI [Gibco, cat #: 11875093], 20% qualified FBS [Gibco, cat #: 26140079], 0.1mM penicillin-streptomycin [Gibco, cat #: 15140122], 1mM sodium pyruvate [Gibco, cat #: 11360070], 2mM L-glutamine [Gibco, cat #: 25030081], 100μM β-mercaptoethanol [Sigma-Aldrich, cat #: 63689]) supplemented with 25 ng/mL FGF4 (Gibco, cat #: PHG0154) and 1 μg/mL Heparin (Sigma-Aldrich, cat #: H3149) just before use, at 37°C in a humidified incubator at 5% CO_2. At passage, TSCs were trypsinized with 0.125% Trypsin-EDTA in PBS solution (Gibco, cat #: 25200–072) for ~4 min at room temperature and gently dislodged from the plate with a sterile, cotton-plugged Pasteur pipette. To deplete irMEFs from TSCs prior to all harvests, TSCs were pre-plated for 45 min at 37°C, transferred to a fresh culture plate, and then cultured for three days in 70% irMEF-conditioned TSC media supplemented with growth factors as above.

ESC culture—Mouse E14 ESCs were cultured on gelatin-coated plates in ESC media (DMEM high glucose and sodium pyruvate [Gibco, cat #: 11995073], 15% qualified FBS, 0.1mM MEM non-essential AA [Gibco, cat #: 11140050], 0.1mM penicillin-streptomycin, 2mM L-glutamine, 100μM β-mercaptoethanol, 1:500 LIF) at 37°C in a humidified incubator with 5% CO_2. At passage, ESCs were trypsinized with 0.125% Trypsin-EDTA in PBS

solution for ~5 min at room temperature and dislodged from the plate at single-cell suspension. ESCs were passaged every other day and provided fresh media daily.

Generation of regulatory element deletions—Per regulatory element deletion, four unique sgRNAs were designed using CRISPOR,[66] with two sgRNAs flanking the target site (Figures S2A–S2D, Table S5). As a negative control, an sgRNA using a non-targeting (NTG) sequence from (Invitrogen, cat #: A35526) was designed. Each sgRNA was cloned into the *BsmbI* site of the piggyBac-cargo rtTA vector (PB_rtTA_BsmBI) from[55] and transformed in DH5-alpha competent bacterial cells. Starter transformant cultures for each sequence-verified sgRNA were pooled together in equal volume amounts prior to liquid culture expansion and plasmid purification using the PureLink HiPure Plasmid Midiprep kit (Invitrogen, cat #: K2100004). The pooled sgRNAs were then co-electroporated with doxycycline-inducible Cas9-cargo (PB_tre_Cas9) and pUC19-piggyBac transposase vectors from[55] at an 8:2:1 plasmid ratio of 2.5μg total DNA into 1 million C/B TSCs on irradiated drug-resistant MEFs (irDR4-MEFs; ATCC, cat #: SCRC-1045) in a single well of a 6-well plate. The electroporations were performed using a Neon Instrument (electroporation settings: 950V, 30ms, 2 pulses). Two days after electroporation, TSCs were selected with 150 μg/mL hygromycin B (Corning, cat #: MT30240CR)) and 200 μg/mL G418 (Gibco, cat #: 10131035) in irMEF-conditioned TSC media with growth factors for 11 days, followed by four days of 1 μg/mL doxycycline treatment (Sigma-Aldrich, cat #: D9891) to induce Cas9 expression. 2,000 doxycycline-induced TSCs were then plated onto a pre-plated irMEFs 100-mm dish for clonal selection and expansion. Prior to harvesting for genotyping assays, clonal TSC lines were passaged once off of irMEFs as above.

For genotyping assays, PCR was used to detect the presence or absence of target deletion DNA. “Wildtype” primers were designed to amplify either the flanking end or internal region of the deletion site. “Deletion” primers were designed to externally flank both ends of the deletion sites that would efficiently amplify a sizable PCR product if the deletion occurred (Table S5). Sanger sequencing (Eton) was then used to detect the presence of informative B6/CAST SNPs in the PCR products for allelic identification.

Generation of Airn-overexpressing ESCs—750,000 ESCs were seeded in a single gelatin-coated well of a six-well plate, and the next day transfected with 2.5μg of an 8:2:1 plasmid ratio of piggyBac-cargo rtTA-*Airn* sgRNA, doxycycline-inducible piggyBac-cargo dCas9-VP160 (PB_tre_dCas9_VP160), and pUC19-piggyBac transposase from[55] using Lipofectamine 3000 (Invitrogen, cat #: L3000015) according to manufacturer instructions. The next day, transfected ESCs were selected with ESC media containing 150 μg/mL hygromycin B and 200 μg/mL G418 for 10 days, followed by 4 days of doxycycline treatment to induce *Airn* expression via dCas9-VP160 prior to harvests.

METHOD DETAILS

***In situ* Hi-C—**Prior to crosslinking for Hi-C, TSCs were passaged once off of irMEFs as described above. TSCs were then trypsinized and washed once with PBS. 5–10 million cells were crosslinked in resuspension with 10mL of 1% formaldehyde (Thermo Scientific, cat #: 28906) in PBS solution for 10 min at room temperature, quenched with 200mM glycine

for 5 min at room temperature, and then washed twice with ice-cold PBS. Cells were then divided into 5 aliquots (1–2 million cells/aliquot), where one aliquot was used for each Hi-C experiment. Importantly, for the removal of all PBS washes and crosslinking solution, cells were spun at 160 × g for 5 min.

Hi-C libraries from C/B wild-type, B/C wild-type, and C/B *Aim* truncation TSCs were generated and sequenced as in the detailed protocol from,[26] including DNA fragmentation with *MboI* and *MseI* restriction enzymes. Hi-C libraries from regulatory element deletion TSCs were generated using the Arima-HiC + kit (Arima Genomics, cat #: A510008) according to the manufacturer instructions. Paired-end, 150-bp sequencing was performed using Illumina NovaSeq 6000 System.

(Calibrated) ChIP-seq—Prior to crosslinking for ChIP, TSCs were passaged once off of irMEFs as above. For all ChIP experiments, except those for PRC components, adhered cells were crosslinked with 0.6% formaldehyde (Fisher Scientific, cat #: BP531–500) in RPMI media with 10% FBS for 10 min at room temperature, then quenched with 125mM glycine for 5 min at room temperature. Crosslinked cells were then washed twice with ice-cold PBS and scraped with ice-cold PBS with 0.05% Tween (Fisher Scientific, cat #: EW-88065–31) and PIC (Sigma Aldrich, cat #: P8340). The cells were then spun at 1,200 × g at 4°C to remove PBS, followed by resuspension in ice-cold PBS with PIC and divided into 10-million cell aliquots. For PRC component ChIPs, adhered C/B TSCs were crosslinked in PBS with 2mM DSG (disuccinimidyl glutarate; Thermo Scientific, cat #: 20593) for 45 min at room temperature and then in PBS with 1% formaldehyde (Thermo Scientific, cat #: 28906) for 15 min at room temperature. Crosslinking was quenched with 200mM glycine for 5 min at room temperature. Cells were then washed, scraped, and aliquoted as above. All ChIPs were performed using 10 million cells, 10μL of antibody, and 30μL of Protein A/G agarose beads (Santa Cruz, cat #: sc-2003). Input chromatin was isolated accordingly to each antibody (see below) and sonicated to 100–500bp fragments using a Vibra-Cell VX130 (Sonics) with the following parameters: 8–10 cycles of 30% intensity for 30 s with 1 min of rest on ice between cycles. Antibody-conjugated beads were prepared by incubating antibody with beads in 300μL Blocking Buffer (PBS, 0.5% BSA [Invitrogen, cat #: AM2616]) overnight at 4°C with rotation.

For H3K27me3 and H2AK119ub ChIPs, crosslinked TSCs were resuspended in 1mL Lysis Buffer 1 (50mM HEPES pH 7.5, 140mM NaCl, 1mM EDTA, 10% glycerol, 0.5% NP-40, 0.25% Triton X-100, PIC) and incubated with rotation for 10 min at 4°C. Cells were then resuspended in 1mL Lysis Buffer 2 (10mM Tris-HCl pH 8.0, 200mM NaCl, 1mM EDTA, 0.5 mM EGTA, PIC) for 10 min at room temperature. All buffer removal steps were performed with 5-min 1,200 × g spins at 4°C. The extracted nuclei pellet was then resuspended and sonicated in 500μL Lysis Buffer 3 (10mM Tris-HCl pH 8.0, 100mM NaCl, 1mM EDTA, 0.5mM EGTA, 0.1% sodium-deoxycholate, 0.5% N- lauroylsarcosine, PIC). Soluble chromatin was obtained with a 30-min max speed spin at 4°C, mixed with 1% Triton X-100, and then incubated with pre-conjugated antibody beads overnight at 4°C with rotation. The ChIP beads were then washed five times in 1mL RIPA Buffer (50mM HEPES pH 7.5, 500mM LiCl, 1mM EDTA, 1% NP-40, 0.7% sodium-deoxycholate, PIC) and once

with 1mL TE, each for 5 min at 4°C with rotation and spun at 2,000 × g for 2 min for buffer removal.

For PRC component ChIPs, crosslinked C/B TSCs were resuspended and sonicated in 500μL Low Salt Pol II ChIP Buffer (50mM Tris-HCl pH 7.5, 140mM NaCl, 1mM EDTA, 1mM EGTA, 0.1% sodium-deoxycholate, 0.1% SDS, PIC). Soluble chromatin was obtained with a 30-min max speed spin at 4°C, mixed with 1% Triton X-100, and then incubated with pre-conjugated antibody beads overnight at 4°C with rotation. The ChIP beads were then washed three times with 1mL Low Salt Pol II ChIP Buffer with 1% Triton X-100 and PIC, once with 1mL High Salt Pol II ChIP Buffer (50mM Tris-HCl pH 7.5, 500mM NaCl, 1mM EDTA, 1mM EGTA, 0.1% sodium-deoxycholate, 0.1% SDS, PIC), once with 1mL LiCl Wash Buffer (20mM Tris-HCl pH 8.0, 250mM LiCl, 1mM EDTA, 0.5% Nadeoxycholate, 0.5% NP-40, PIC), and once with 1 mL TE, each for 5 min at 4°C with rotation and spun at 2,000 × g for 2 min for buffer removal.

For all ChIP DNA elution steps, washed beads were resuspended in Elution buffer (50mM Tris-HCl pH 8.0, 10mM EDTA, 1% SDS) and placed on a 65°C heat block for 17 min with frequent vortexing. ChIP DNA was then reverse crosslinked in 0.5% SDS and 100mM NaCl overnight at 65°C, followed by a 1-h RNaseA (3μL; Thermo Scientific, cat #: EN0531) treatment at 37°C and a 2.5-h Proteinase K (10μL; Invitrogen, cat #: 25530015) treatment at 56°C. DNA was then extracted with 1 volume of phenol:chloroform:isoamyl alcohol (Sigma-Aldrich, cat #: P3803) and precipitated with 2 volumes 100% ethanol, 1/10 volume 3M sodium-acetate pH 5.4, and 1/1000 volume linear acrylamide (Invitrogen, cat #: AM9520) overnight at −20°C. Precipitated DNA was then extracted with a 30-min max speed spin at 4°C, washed once with ice-cold 80% ethanol, and resuspended in TE.

Calibrated ChIPs were performed to validate *Airn*-induced changes across genotypes. At the IP step, 5% sonicated chromatin from HEK293T cells was added to a standardized protein amount of input TSC chromatin across samples. Bradford protein assays (Bio-Rad, cat #: 5000006) with BSA protein standard were performed to determine protein quantity as a proxy for input chromatin amount. HEK293T chromatin was sonicated as above to achieve 100–500bp fragments. All other steps were performed as normal.

ChIP-seq libraries were prepared with NEBNext End Repair Module (NEB, cat #: E6050S), A-tailing by Klenow Fragment (3'→5′ exo-; NEB, cat #: M0212S), and TruSeq 6-bp index adaptor ligation by Quick ligase (NEB, cat #: M2200S), and NEBNext High-Fidelity 2X PCR Master Mix (NEB, cat #: M0541S). All DNA size-selection purification steps were performed with AMPure XP beads (Beckman Coulter, cat #: A63880). Single-end, 75-bp sequencing was performed using an Illumina NextSeq 500/550 High Output v2.5 kit (Illumina, cat #: 20024906) on a NextSeq 500 System.

CHART-seq—CHART was performed in duplicate as in the detailed protocol from.[67] TSCs were passaged once off of irMEFs as above. *Airn* highly-expressing TSCs from[14] and ESCs were induced with 1 μg/mL doxycycline 4 days prior to crosslinking. Adhered TSCs and ESCs were crosslinked with 1% formaldehyde (Fisher Scientific, cat #: BP531–500) in PBS solution for 10 min at room temperature. On ice, cells were washed twice with ice-cold PBS

and twice with ice-cold PBS +0.05% Tween before being scraped, spun at 1,000 × g for 5 min at 4°C, and divided into 25-million cell aliquots.

Per aliquot, nuclei was extracted with two rounds of douncing in 4mL sucrose buffer (300mM sucrose, 10mM HEPES pH 7.5, 100mM KOAc, 1% Triton X-100, 0.1mM EGTA, 0.5mM spermidine, 0.15mM spermine, cOmplete EDTA-free protease inhibitor cocktail [Millipore, cat #: 11873580001], 1mM DTT, 80U SUPERase-in [Invitrogen, cat #: AM2696]), mixing 1:1 with glycerol buffer (25% glycerol, 10mM HEPES pH 7.5, 100mM KOAc, 1mM EDTA, 0.1mM EGTA, 0.5mM spermidine, 0.15mM spermine, cOmplete EDTA-free protease inhibitor cocktail, 1mM DTT, 80U SUPERase-in), and centrifugation through 4mL glycerol buffer at 1,000 × g for 15 min at 4°C. The nuclei pellet was then washed twice with ice-cold PBS +0.05% Tween, then further crosslinked with 3% formaldehyde (Fisher Scientific, cat #: BP531–500) in PBS +0.05% Tween for 30 min at room temperature. Formaldehyde was then washed out twice with ice-cold PBS +0.05% Tween, then resuspended in freshly prepared 250μL Sonication Buffer (50mM HEPES pH 7.5, 75mM NaCl, 0.5% *N*-lauroylsarcosine solution, 0.1% sodium-deoxycholate, 0.1mM EGTA, cOmplete EDTA-free protease inhibitor cocktail, 1mMDTT, 300U SUPERase-in). Chromatin was sonicated to 2–10kb fragments using a Bioruptor Plus sonication device (Diagenode; sonication parameters: 30 s on, 30 s off cycles on high setting), then spun at max speed for 30 min at 4°C to retrieve soluble chromatin.

For *Airn* CHART, we designed 22-nucleotide complementary oligos that tile across the first 75 kb of the *Airn* RNA sequence using the ChIRP Probe Designer (LGC Biosearch Technologies) under parameters of high masking for specificity and ≥500-nt spacings (Table S5). The resulting 51 oligo probes were then mixed to a 100μM pool for in-house oligo biotin labeling.[68] Briefly, 20μM oligo probe mix was labeled with 300μM biotin-16-dUTP (Roche, cat #: 11093070910) and 30U terminal deoxynucleotidyl transferase (Thermo Scientific, cat #: EP0161), then labeled for 15 min at 37°C and inactivated for 20 min at 75°C. Biotinylated oligo probes were then purified using the QIAquick Nucleotide Removal kit (Qiagen, cat #: 28304), eluting to ~20μM.

Per *Airn* CHART reaction, 12.5 million cells worth of chromatin was mixed with 0.5 volume PAB (8M Urea, 100mM HEPES pH 7.5, 200mM NaCl, 2% SDS) and 1.5 volumes of freshly prepared Hybridization Buffer (1.5M NaCl, 1.12M Urea, 10X Denhardt's solution [Invitrogen, cat #: 750018], 10mM EDTA), then pre-cleared with 50μL Dynabeads M-280 Streptavidin beads (Invitrogen, cat #: 11205D) for 1 h at room temperature with rotation. The pre-cleared chromatin was then isolated from the beads by spinning at 1,000 × g for 30 s. 1% of pre-cleared chromatin was saved as "Input" sample, and the remaining pre-cleared chromatin was incubated with 750pmol biotinylated oligo probes overnight at room temperature. The next day, the sample was spun at max speed for 20 min at 20°C, and the supernatant was incubated with 200μL worth of Dynabeads MyOne Streptavidin C1 beads (Invitrogen, cat #: 65001) resuspended in 125μL 2:1 diluted PAB overnight at room temperature with rotation. CHART beads were then placed on the magnet and washed 4 times with 400μL CHART Wash Buffer (250mM NaCl, 10mM HEPES pH 7.5, 2mM EDTA, 2mM EGTA, 0.2% SDS, 0.1% *N*-lauroylsarcosine) and once with RNase H Elution Buffer (75mM NaCl, 50mM HEPES pH 7.5, 0.02% sodium-deoxycholate, 0.1% *N*-

lauroylsarcosine, 10mM DTT, 3mM $MgCl_2$, 200U SUPERase-in). Beads were resuspended in 100μL RNase H Elution Buffer and treated with 2μL RNase H (NEB, cat #: M0297) for 10 min at room temperature. To stop the RNase H reaction, 1/4 volume of naXLR (166.7mM Tris-HCl pH 7.2, 1.67% SDS, 83.3mM EDTA, 600μg Proteinase K [Bioline, cat #: BIO-37084]) was added, and the CHART eluate was then subject to proteinase K digestion and reverse-crosslinking for 1 h at 55°C, followed by 1h at 65°C. The sample was then split for DNA (90%) and RNA (10%) analysis.

The *Airn* CHART-enriched RNA sample was treated with 1mL TRIZol and 200μL chloroform, and the RNA was DNase-treated and purified with Zymo Research RNA Clean & Concentrator kit (Zymo Research, cat #: 50–125-1669). To determine the extent of *Airn* RNA enrichment, 50% of both Input and CHART RNA samples were reverse transcribed using High-Capacity cDNA Reverse Transcription Kit (Applied Biosystems, cat #: 4368814). qPCR was performed using iTaq Universal SYBR Green Supermix (Bio-Rad, cat #: 1725125) and primers targeting 45 kb downstream of the *Airn* TSS and *Gapdh* (Table S5).

The *Airn* CHART-enriched DNA sample was extracted with 1 volume of phenol:chloroform:isoamyl and purified with ethanol precipitation and TE resuspension as above for ChIP DNA. qPCR was performed as above with the same primers to check *Airn* DNA enrichment.

CHART-seq libraries were prepared as above for ChIP-seq libraries. However, prior to library prep, CHART-enriched DNA samples were further sonicated to 100–500bp fragments using the Bioruptor Plus with 10 cycles of 30 s on, 30 s off on high setting, then purified with one round of 1:1 AMPure XP beads size selection purification. Single-end, 75-bp sequencing was performed using an Il-lumina NextSeq 500/550 High Output v2.5 kit on a NextSeq 500 System.

RNA isolation, RT-qPCR, RNA-seq—TSCs were passaged once off of irMEFs as above onto a single well of a 6-well plate. ESCs were grown on a single well of a 6-well plate. Both were grown to ≥75% confluency prior to RNA harvest using 1mL TRIzol, followed by the addition of 200μL chloroform, which were vortexed and subsequently spun at max speed for 5 min at 4°C for phase separation. The aqueous layer was collected and combined with 1 volume of 100% isopropanol and 5μL linear acrylamide. Precipitation was achieved at −80°C for 1 h, followed by a max speed spin for 30 min at 4°C and one wash of the RNA pellet with ice-cold 80% ethanol. The pellet was then resuspended in 100μL H_2O and quantified via Qubit (Invitrogen, cat #: Q32855).

For RT-qPCR assays in Figures 5A and S4E, 1μg of RNA was reverse transcribed using the High-Capacity cDNA Reverse Transcription Kit, and qPCR was performed using iTaq Universal SYBR Green Supermix and custom primers (Table S5).

RNA-seq libraries were prepared from 1μg of total RNA using KAPA RNA HyperPrep Kit with Ribose Erase (Kapa Biosystems, cat #: KR1351) according to the manufacturer

instructions. Single-end, 75-bp sequencing was performed using an Illumina NextSeq 500/550 High Output v2.5 kit on a NextSeq 500 System.

Sequence alignment and processing—All mouse reference NCBI build 37/mm9 genome annotations were obtained from the UCSC genome browser.[69] Variant sequence data was obtained from the Sanger Institute (http://www.sanger.ac.uk/resources/mouse/genomes/.[25]; The CAST/EiJ (CAST) pseudogenome creation was performed as in.[40,64] Hi-C reads were aligned using BWA as a part of the Juicer pipeline (Durand et al. 2016a). ChIP- and CHART-seq reads were aligned using bowtie2 with default parameters.[70] RNA-seq reads were aligned using STAR with default parameters.[58]

For Hi-C analyses in this study, read pairs that had a mapping quality greater than or equal to 10 were used for allelic TSC analysis and read pairs that had greater than or equal to 30 were used for ESC analysis. For all ChIP-, CHART- and RNA-seq analyses in this study, reads that had a mapping quality greater than or equal to 30 were extracted with samtools,[59] and allele-specific read retention (i.e., reads that overlap at least one B6 or CAST SNP) was performed as in[40,64] using a custom perl script (intersect_reads_snps16.pl: see github).

Chromosome tiling density plots—For all chromosome-scale tiling density plots in Figures 2–6 and S2–S6, reads were summed in 10kb bins across each chromosome. MAPQ≥30 aligned reads were then divided by the total number of reads in the dataset and divided by a million (i.e., RPM). For allelic TSC ChIP- and CHART-seq data, binned counts were divided by the number of B6/CAST SNPs detected in the bin genomic coordinates (i.e., SNP-norm RPM). Finally, bins were averaged every 9 bins in 1bin increments. For allelic TSC Hi-C viewpoint data, we excluded bins whose aggregate SNP-overlapping read count across merged Hi-C datasets fell within the bottom quintile relative to bins in the rest of the genome. The allelic data in this group of bins were too sparse to be interpreted with confidence. For the same reason, for allelic CHART- and ChIP-seq data, only bins with greater or equal to 25 SNPs were plotted. Bins of replicate datasets were averaged.

For total, non-allelic ESC *Airn* CHART-seq and H3K27me3 ChIP-seq data, reads were RPM converted, binned, and averaged as above. For all ESC data in Figure 4, the same genomic bins as the allelic TSC ChIP- and CHART-seq data were plotted.

All plots were generated using ggplot2[63] in RStudio.

Tiling density correlations—To derive Spearman's r and p values for tiling density correlations in Figures 2 and 4, reads were processed as described in "Chromosome tiling density plots" and every 10th bin along the genomic region of interest was correlated.

To determine significant changes in H3K27me3 and H2AK119ub density across genotypes in Figures 5 and S6, all binned SNP-norm RPM values over the genomic region of analysis were subjected to a Welch two-sample t test in RStudio.

Genome browser density tracks—Wiggle density files were created using a custom perl script (bigbowtie_to_wig3_mm9.pl; see github) and loaded into a UCSC Genome

Browser session to generate the graphics in Figures 3 and 7. All density tracks were auto-scaled to data view and set to a maximum windowing function with 3-pixel smoothing.

Hi-C analysis

Juicer processing, quality control, and allele-specific read retention: Hi-C analyses were carried out using a combination of Juicer (default parameters) and HiCExplorer.[27,57,71] For exact Juicer commands used, see github.

For quality control, Hi-C statistics of each dataset were generated by Juicer (Table S1) and were referenced to the standard guidelines in.[26] In addition, long-range DNA interactions (25kb-10Mb) were correlated between Hi-C replicate datasets at 10kb and 25kb resolutions using HiCExplorer's hicCorrelate[56] with the following parameters: –method = pearson –range 25000:10000000.

For allele-specific retention of Hi-C contacts, read pairs in which at least one read end overlaps a B6/CAST SNP were extracted from the Juicer output merged_nodups.txt file using a modified Juicer diploid script (juicer_diploid_v6.sh; see github).

2D contact heatmaps: Allelic 2D contact heatmaps in Figures 1, 6, 7, S1 and S7 were generated with Juicebox.[71] Contact matrices of observed counts were viewed in KR (Knight-Ruiz) balance mode at 5kb and 50kb resolutions. Subtraction heatmaps, where maternal contacts were subtracted from paternal contacts, were viewed under the same conditions.

Loop calling: DNA loops were detected using the Significant Interaction Peak (SIP) caller[43] with the following parameters: -factor 4 -g 2.0 -t 2000 -fdr 0.05. The output finalLoops.txt file (i.e., a merged list of unique DNA loop anchors detected across 5k, 10kb, and 25kb resolutions) was used to determine loops over the 2D contact heatmaps in Juicebox for Figure 7.

"A" and "B" compartmentalization: "A" and "B" chromosome compartments for each allele were delineated by eigenvector analysis using the Juicer *eigenvector* tool with the following parameters: -p KR 17 BP 50000. Extracted eigenvector values were then visualized and plotted with Juicebox in Figures 1 and 6.

Allelic viewpoints: Allelic viewpoints of locus-specific contact matrices were extracted at 10 or 25kb resolution for observed and observed-over-expected (O/E) counts using the Juicer *dump* tool with the following parameters: observed/oe NONE chr:start:end chr:start:end BP 10000/25000. If applicable, all viewpoint loci of interest were extended to 100kb lengths from their centers to improve contact matrix coverage. Extracted counts were then processed and plotted as described in the Chromosome-scale tiling density plots section.

Correlation with FISH: Allelic observed contacts from *Airn* viewpoint data in C/B wild-type TSCs were summed over the genomic coordinates for each of the 9 FISH probes across the *Airn* target domain analyzed in.[14] For each allele, the summed Hi-C counts at the probe

locations were then correlated by Spearman's test (using in RStudio) with the corresponding average distance to the *Airn* probe as measured by RNA/DNA co-FISH in C/B TSCs.[14] Scatterplots in Figure 2 were generated with ggplot2 in RStudio.[63]

ChIP-seq analysis

Calibrated ChIP-seq spike-in normalization: Reads from calibrated ChIP-seq samples were also aligned to human GRCh37/hg19 genome build. A normalization factor was calculated for each sample using the formula 1/h, where h is the number of hg19-aligned reads in millions, as described previously.[72,73] Raw B6 and CAST reads were then scaled by multiplying the corresponding normalization factor. For tiling density plots, binned spike-in normalized reads were divided by the total number of B6/CAST SNPs.

Peak calling: ChIP-seq peaks were called from non-allelic reads against an H3 ChIP-seq dataset (from[40]) using the MACS2 peak calling algorithm[61] with the following parameters: -g mm –broad –broad-cutoff 0.01.

Allelic enrichment at CpG islands and other features: A statistical permutation test was performed to determine how significantly enriched PRC components, CTCF, SMC1A/Cohesin, and epigenetic marks are at loci of interest relative to the rest of the genome (see Table S3). All datasets analyzed were generated from C/B TSCs. H3K27ac, H3K4me2, CTCF, and SMC1A data were generated in previous studies, as a part of.[14,40] If applicable, all genomic features of interest were standardized to 1.5kb lengths (i.e., the largest CGI of interest) relative to their center positions. Using bedtools' 'shuffle',[60] we created a list of 80,000 1.5kb regions randomly selected from within 'gene' coordinates from gencode.v-M1.annotation.gtf[74] with 100kb extended start and end sites while excluding any regions that fell within 2.5kb of a region annotated by MACS as an H3K27me3 or PRC subunit peak. Shuffled coordinates were filtered to retain regions encompassing at least one B6/CAST SNP, leaving 67,262 shuffled regions. B6- and CAST-overlapping ChIP-seq reads were then counted over the features of interest and shuffled coordinates using a custom script (ase_analyzer10_adj2.pl; see github), then divided by the number of B6/CAST SNPs detected in the genomic coordinates (SNP-norm counts). The features were then ranked by SNP-norm counts for each allele in each dataset (1 = highest allelic signal), and a percentile rank was used to determine an empirical p value for allele-specific enrichment of the ChIP target at the loci of interest.

RNA-seq analysis—For non-allelic expression analysis in Table S2, featureCounts[62] was used to count reads over 'gene' entries in gencode.vM1.annotation.gtf.[74] Counts were then divided by total reads in the dataset and divided by a million (RPM).

For allelic expression analysis in Table S2 and Figures 5 and S6, a custom perl script (ase_analyzer10.pl; see github) was used to count B6- and CAST SNP-overlapping reads over 'gene' entries in gencode.vM1.annotation.gtf.[74] Read counts were divided by the total number of reads in the dataset, divided by a million, and divided by the number of SNPs detected within the 'gene' coordinates (SNP-norm RPM). To determine the relative paternal expression of *Airn* in Figure S5E, paternal SNP-norm RPM values over *Airn* for each

genotype were divided by was divided by the averaged NTG value from all four NTG clone data. To determine the relative paternal bias of *Airn* target gene expression for each genotype in Figure 5, paternal SNP-norm RPM values for the 27 *Airn* target genes (Table S2;[14]) were divided by the sum of the paternal and maternal values. The paternal biases for each genotype were then divided by the averaged NTG value from all four NTG clone data, and a Welch t test was used to determine the p value of the relative change in expression relative to NTG in RStudio. Boxplots of these data were generated using GraphPad Prism v9.

QUANTIFICATION AND STATISTICAL ANALYSIS

In Figure 2B, we used Spearman's Rank Correlation to determine the relationship between KR-balanced Hi-C counts with the *Airn* viewpoint (normalized for SNP density) versus our previous measurements of spatial distance to the *Airn* locus made by DNA FISH in.[14] In Figure 2F, we used Spearman's Rank Correlation to determine the relationship between KR-balanced Hi-C counts with the *Airn* viewpoint (normalized for SNP density) and the density of H3K27me3 and H2AK119ub on the paternal allele. In Figure 3, we used an empirical sampling of ChIP-seq read density in intergenic regions to determine the likelihood that each analyzed histone modification and chromatin-associated factor was enriched within a given region above what we would have expected by chance ($p < 0.05$). In Figures 4B–4D, we used Spearman's Rank Correlation to determine the relationship the density of *Airn* CHART-seq signal on the paternal allele and H3K27me3, RING1B, and EZH2 ChIP-seq signal, respectively, also on the paternal allele. In Figure 4F, we used Spearman's Rank Correlation to determine the relationship the density of *Airn* CHART signal and H3K27me3 in ESCs (non-allelic). In Figure 5E, we used a Welch two-sample t test to determine the likelihood ($p < 0.05$) that the relative paternal bias of 27 Airn target genes from[14] changed in each individual genotype relative to NTG control. In Figure 7D, we also used a Welch t test to determine the likelihood that the allelic H3K27me3 and H2AK119ub density was altered in the Δ*Slc22a3* and Δ*Pde10a* genotypes relative to the NTG control. Throughout our study, the term "n" refers to a biological replicate. Statistical analyses were performed in R. Software packages used are listed in the key resources table. Additional details can be found in the figure legends, the body of the manuscript, and in the method details section above.

Supplementary Material

Refer to Web version on PubMed Central for supplementary material.

ACKNOWLEDGMENTS

This work was supported by NIH grants R01GM136819 (to J.M.C.), UM1HG009375 (to E.L.A.), R35GM128645 (to D.H.P.), and R35GM124764 (to J.M.D.); NICHD grant F31HD103370 (to A.K.B.); and NIGMS grants T32GM119999 (to A.K.B.), T32CA217824 (to J.B.T.), and T32GM067553 (to E.S.D.).

REFERENCES

1. Monk D, Mackay DJG, Eggermann T, Maher ER, and Riccio A (2019). Genomic imprinting disorders: lessons on how genome, epigenome and environment interact. Nat. Rev. Genet. 20, 235–248. 10.1038/s41576-018-0092-0. [PubMed: 30647469]

2. Tucci V, Isles AR, Kelsey G, and Ferguson-Smith AC; Erice Imprinting Group (2019). Genomic Imprinting and Physiological Processes in Mammals. Cell 176, 952–965. 10.1016/j.cell.2019.01.043. [PubMed: 30794780]

3. MacDonald WA, and Mann MRW (2020). Long noncoding RNA functionality in imprinted domain regulation. PLoS Genet. 16, e1008930. 10.1371/journal.pgen.1008930. [PubMed: 32760061]

4. Llères D, Imaizumi Y, and Feil R (2021). Exploring chromatin structural roles of non-coding RNAs at imprinted domains. Biochem. Soc. Trans. 49, 1867–1879. 10.1042/BST20210758. [PubMed: 34338292]

5. Huang R, Jaritz M, Guenzl P, Vlatkovic I, Sommer A, Tamir IM, Marks H, Klampfl T, Kralovics R, Stunnenberg HG, et al. (2011). An RNA-Seq strategy to detect the complete coding and non-coding transcriptome including full-length imprinted macro ncRNAs. PLoS One 6, e27288. 10.1371/journal.pone.0027288. [PubMed: 22102886]

6. Lyle R, Watanabe D, te Vruchte D, Lerchner W, Smrzka OW, Wutz A, Schageman J, Hahner L, Davies C, and Barlow DP (2000). The imprinted antisense RNA at the Igf2r locus overlaps but does not imprint Mas1. Nat. Genet. 25, 19–21. 10.1038/75546. [PubMed: 10802648]

7. Terranova R, Yokobayashi S, Stadler MB, Otte AP, van Lohuizen M, Orkin SH, and Peters AHFM (2008). Polycomb group proteins Ezh2 and Rnf2 direct genomic contraction and imprinted repression in early mouse embryos. Dev. Cell 15, 668–679. 10.1016/j.devcel.2008.08.015. [PubMed: 18848501]

8. Sleutels F, Zwart R, and Barlow DP (2002). The non-coding Air RNA is required for silencing autosomal imprinted genes. Nature 415, 810–813. 10.1038/415810a.415810a [pii]. [PubMed: 11845212]

9. Killian JK, Nolan CM, Wylie AA, Li T, Vu TH, Hoffman AR, and Jirtle RL (2001). Divergent evolution in M6P/IGF2R imprinting from the Jurassic to the Quaternary. Hum. Mol. Genet. 10, 1721–1728. 10.1093/hmg/10.17.1721. [PubMed: 11532981]

10. Yotova IY, Vlatkovic IM, Pauler FM, Warczok KE, Ambros PF, Oshimura M, Theussl HC, Gessler M, Wagner EF, and Barlow DP (2008). Identification of the human homolog of the imprinted mouse Air non-coding RNA. Genomics 92, 464–473. 10.1016/j.ygeno.2008.08.004. [PubMed: 18789384]

11. Suzuki S, Shaw G, and Renfree MB (2018). Identification of a novel antisense noncoding RNA, ALID, transcribed from the putative imprinting control region of marsupial IGF2R. Epigenet. Chromatin 11, 55. 10.1186/s13072-018-0227-8.

12. Seidl CIM, Stricker SH, and Barlow DP (2006). The imprinted Air ncRNA is an atypical RNAPII transcript that evades splicing and escapes nuclear export. EMBO J. 25, 3565–3575. 10.1038/sj.emboj.7601245. [PubMed: 16874305]

13. Andergassen D, Dotter CP, Wenzel D, Sigl V, Bammer PC, Muckenhuber M, Mayer D, Kulinski TM, Theussl HC, Penninger JM, et al. (2017). Mapping the mouse Allelome reveals tissue-specific regulation of allelic expression. Elife 6, e25125. 10.7554/eLife.25125. [PubMed: 28806168]

14. Schertzer MD, Braceros KCA, Starmer J, Cherney RE, Lee DM, Salazar G, Justice M, Bischoff SR, Cowley DO, Ariel P, et al. (2019). lncRNA-Induced Spread of Polycomb Controlled by Genome Architecture, RNA Abundance, and CpG Island DNA. Mol. Cell. 75, 523–537.e10. 10.1016/j.molcel.2019.05.028. [PubMed: 31256989]

15. Latos PA, Pauler FM, Koerner MV, Sxenergin HB, Hudson QJ, Stocsits RR, Allhoff W, Stricker SH, Klement RM, Warczok KE, et al. (2012). Airn transcriptional overlap, but not its lncRNA products, induces imprinted Igf2r silencing. Science 338, 1469–1472, 338/6113/1469 [pii]. 10.1126/science.1228110. [PubMed: 23239737]

16. Pauler FM, Barlow DP, and Hudson QJ (2012). Mechanisms of long range silencing by imprinted macro non-coding RNAs. Curr. Opin. Genet. Dev. 22, 283–289. 10.1016/j.gde.2012.02.005. [PubMed: 22386265]

17. Andergassen D, Muckenhuber M, Bammer PC, Kulinski TM, Theussl HC, Shimizu T, Penninger JM, Pauler FM, and Hudson QJ (2019). The Airn lncRNA does not require any DNA elements within its locus to silence distant imprinted genes. PLoS Genet. 15, e1008268. 10.1371/journal.pgen.1008268. [PubMed: 31329595]

18. Nagano T, Mitchell JA, Sanz LA, Pauler FM, Ferguson-Smith AC, Feil R, and Fraser P (2008). The Air noncoding RNA epigenetically silences transcription by targeting G9a to chromatin. Science 322, 1717–1720, 1163802 [pii]. 10.1126/science.1163802. [PubMed: 18988810]
19. Grosswendt S, Kretzmer H, Smith ZD, Kumar AS, Hetzel S, Wittler L, Klages S, Timmermann B, Mukherji S, and Meissner A (2020). Epigenetic regulator function through mouse gastrulation. Nature 584, 102–108. 10.1038/s41586-020-2552-x. [PubMed: 32728215]
20. Andergassen D, Smith ZD, Kretzmer H, Rinn JL, and Meissner A (2021). Diverse epigenetic mechanisms maintain parental imprints within the embryonic and extraembryonic lineages. Dev. Cell 56, 2995–3005.e4. 10.1016/j.devcel.2021.10.010. [PubMed: 34752748]
21. Trotman JB, Braceros KCA, Cherney RE, Murvin MM, and Calabrese JM (2021). The control of polycomb repressive complexes by long noncoding RNAs. Wiley Interdiscip Rev RNA 12, e1657. 10.1002/wrna.1657. [PubMed: 33861025]
22. Blackledge NP, and Klose RJ (2021). The molecular principles of gene regulation by Polycomb repressive complexes. Nat. Rev. Mol. Cell Biol. 22, 815–833. 10.1038/s41580-021-00398-y. [PubMed: 34400841]
23. Almeida M, Pintacuda G, Masui O, Koseki Y, Gdula M, Cerase A, Brown D, Mould A, Innocent C, Nakayama M, et al. (2017). PCGF3/5-PRC1 initiates Polycomb recruitment in X chromosome inactivation. Science 356, 1081–1084. 10.1126/science.aal2512. [PubMed: 28596365]
24. Bousard A, Raposo AC, Żylicz JJ, Picard C, Pires VB, Qi Y, Gil C, Syx L, Chang HY, Heard E, and da Rocha ST (2019). The role of Xist-mediated Polycomb recruitment in the initiation of X-chromosome inactivation. EMBO Rep. 20, e48019. 10.15252/embr.201948019. [PubMed: 31456285]
25. Keane TM, Goodstadt L, Danecek P, White MA, Wong K, Yalcin B, Heger A, Agam A, Slater G, Goodson M, et al. (2011). Mouse genomic variation and its effect on phenotypes and gene regulation. Nature 477, 289–294, nature10413 [pii]. 10.1038/nature10413. [PubMed: 21921910]
26. Rao SSP, Huntley MH, Durand NC, Stamenova EK, Bochkov ID, Robinson JT, Sanborn AL, Machol I, Omer AD, Lander ES, and Aiden EL (2014). A 3D map of the human genome at kilobase resolution reveals principles of chromatin looping. Cell 159, 1665–1680. 10.1016/j.cell.2014.11.021. [PubMed: 25497547]
27. Durand NC, Robinson JT, Shamim MS, Machol I, Mesirov JP, Lander ES, and Aiden EL (2016). Juicebox Provides a Visualization System for Hi-C Contact Maps with Unlimited Zoom. Cell Syst. 3, 99–101. 10.1016/j.cels.2015.07.012. [PubMed: 27467250]
28. Durand NC, Shamim MS, Machol I, Rao SSP, Huntley MH, Lander ES, and Aiden EL (2016). Juicer Provides a One-Click System for Analyzing Loop-Resolution Hi-C Experiments. Cell Syst. 3, 95–98. 10.1016/j.cels.2016.07.002. [PubMed: 27467249]
29. Lieberman-Aiden E, van Berkum NL, Williams L, Imakaev M, Ragoczy T, Telling A, Amit I, Lajoie BR, Sabo PJ, Dorschner MO, et al. (2009). Comprehensive mapping of long-range interactions reveals folding principles of the human genome. Science 326, 289–293, 326/5950/289 [pii]. 10.1126/science.1181369. [PubMed: 19815776]
30. Blackledge NP, Fursova NA, Kelley JR, Huseyin MK, Feldmann A, and Klose RJ (2020). PRC1 Catalytic Activity Is Central to Polycomb System Function. Mol. Cell. 77, 857–874.e9. 10.1016/j.molcel.2019.12.001. [PubMed: 31883950]
31. Boyle S, Flyamer IM, Williamson I, Sengupta D, Bickmore WA, and Illingworth RS (2020). A central role for canonical PRC1 in shaping the 3D nuclear landscape. Genes Dev. 34, 931–949. 10.1101/gad.336487.120. [PubMed: 32439634]
32. Oksuz O, Narendra V, Lee CH, Descostes N, LeRoy G, Raviram R, Blumenberg L, Karch K, Rocha PP, Garcia BA, et al. (2018). Capturing the Onset of PRC2-Mediated Repressive Domain Formation. Mol. Cell. 70, 1149–1162.e5. 10.1016/j.molcel.2018.05.023. [PubMed: 29932905]
33. Isono K, Endo TA, Ku M, Yamada D, Suzuki R, Sharif J, Ishikura T, Toyoda T, Bernstein BE, and Koseki H (2013). SAM domain polymerization links subnuclear clustering of PRC1 to gene silencing. Dev. Cell 26, 565–577. 10.1016/j.devcel.2013.08.016. [PubMed: 24091011]
34. Eeftens JM, Kapoor M, Michieletto D, and Brangwynne CP (2021). Polycomb condensates can promote epigenetic marks but are not required for sustained chromatin compaction. Nat. Commun. 12, 5888. 10.1038/s41467-021-26147-5. [PubMed: 34620850]

35. Kraft K, Yost KE, Murphy SE, Magg A, Long Y, Corces MR, Granja JM, Wittler L, Mundlos S, Cech TR, et al. (2022). Polycomb-mediated genome architecture enables long-range spreading of H3K27 methylation. Proc. Natl. Acad. Sci. USA 119, e2201883119. 10.1073/pnas.2201883119. [PubMed: 35617427]

36. Cai Y, Zhang Y, Loh YP, Tng JQ, Lim MC, Cao Z, Raju A, Lieberman Aiden E, Li S, Manikandan L, et al. (2021). H3K27me3-rich genomic regions can function as silencers to repress gene expression via chromatin interactions. Nat. Commun. 12, 719. 10.1038/s41467-021-20940-y. [PubMed: 33514712]

37. Cuadrado A, Giménez-Llorente D, Kojic A, Rodríguez-Corsino M, Cuartero Y, Martín-Serrano G, Gómez-López G, Marti-Renom MA, and Losada A (2019). Specific Contributions of Cohesin-SA1 and Cohesin-SA2 to TADs and Polycomb Domains in Embryonic Stem Cells. Cell Rep. 27, 3500–3510.e4. 10.1016/j.celrep.2019.05.078. [PubMed: 31216471]

38. Kriz AJ, Colognori D, Sunwoo H, Nabet B, and Lee JT (2021). Balancing cohesin eviction and retention prevents aberrant chromosomal interactions, Polycomb-mediated repression, and X-inactivation. Mol. Cell. 81, 1970–1987.e9. 10.1016/j.molcel.2021.02.031. [PubMed: 33725485]

39. Rhodes JDP, Feldmann A, Hernández-Rodríguez B, Díz N, Brown JM, Fursova NA, Blackledge NP, Prathapan P, Dobrinic P, Huseyin MK, et al. (2020). Cohesin Disrupts Polycomb-Dependent Chromosome Interactions in Embryonic Stem Cells. Cell Rep. 30, 820–835.e10. 10.1016/j.celrep.2019.12.057. [PubMed: 31968256]

40. Calabrese JM, Sun W, Song L, Mugford JW, Williams L, Yee D, Starmer J, Mieczkowski P, Crawford GE, and Magnuson T (2012). Site-specific silencing of regulatory elements as a mechanism of X inactivation. Cell 151, 951–963, S0092–8674(12)01300–1 [pii]. 10.1016/j.cell.2012.10.037. [PubMed: 23178118]

41. Simon MD, Pinter SF, Fang R, Sarma K, Rutenberg-Schoenberg M, Bowman SK, Kesner BA, Maier VK, Kingston RE, and Lee JT (2013). High-resolution Xist binding maps reveal two-step spreading during X-chromosome inactivation. Nature 504, 465–469. 10.1038/nature12719. [PubMed: 24162848]

42. Bonev B, Mendelson Cohen N, Szabo Q, Fritsch L, Papadopoulos GL, Lubling Y, Xu X, Lv X, Hugnot JP, Tanay A, and Cavalli G (2017). Multiscale 3D Genome Rewiring during Mouse Neural Development. Cell 171, 557–572.e24. 10.1016/j.cell.2017.09.043. [PubMed: 29053968]

43. Rowley MJ, Poulet A, Nichols MH, Bixler BJ, Sanborn AL, Brouhard EA, Hermetz K, Linsenbaum H, Csankovszki G, Lieberman Aiden E, and Corces VG (2020). Analysis of Hi-C data using SIP effectively identifies loops in organisms from C. elegans to mammals. Genome Res. 30, 447–458. 10.1101/gr.257832.119. [PubMed: 32127418]

44. Mirny L, and Dekker J (2022). Mechanisms of Chromosome Folding and Nuclear Organization: Their Interplay and Open Questions. Cold Spring Harbor Perspect. Biol. 14, a040147. 10.1101/cshper-spect.a040147.

45. Højfeldt JW, Laugesen A, Willumsen BM, Damhofer H, Hedehus L, Tvardovskiy A, Mohammad F, Jensen ON, and Helin K (2018). Accurate H3K27 methylation can be established de novo by SUZ12-directed PRC2. Nat. Struct. Mol. Biol. 25, 225–232. 10.1038/s41594-018-0036-6. [PubMed: 29483650]

46. Arnold PR, Wells AD, and Li XC (2019). Diversity and Emerging Roles of Enhancer RNA in Regulation of Gene Expression and Cell Fate. Front. Cell Dev. Biol. 7, 377. 10.3389/fcell.2019.00377. [PubMed: 31993419]

47. Statello L, Guo CJ, Chen LL, and Huarte M (2021). Gene regulation by long non-coding RNAs and its biological functions. Nat. Rev. Mol. Cell Biol. 22, 96–118. 10.1038/s41580-020-00315-9. [PubMed: 33353982]

48. Galupa R, Picard C, Servant N, Nora EP, Zhan Y, van Bemmel JG, El Marjou F, Johanneau C, Borensztein M, Ancelin K, et al. (2022). Inversion of a topological domain leads to restricted changes in its gene expression and affects interdomain communication. Development 149, dev200568. 10.1242/dev.200568. [PubMed: 35502750]

49. Greenwald WW, Li H, Benaglio P, Jakubosky D, Matsui H, Schmitt A, Selvaraj S, D'Antonio M, D'Antonio-Chronowska A, Smith EN, and Frazer KA (2019). Subtle changes in chromatin loop contact propensity are associated with differential gene regulation and expression. Nat. Commun. 10, 1054. 10.1038/s41467-019-08940-5. [PubMed: 30837461]

50. Zuin J, Roth G, Zhan Y, Cramard J, Redolfi J, Piskadlo E, Mach P, Kryzhanovska M, Tihanyi G, Kohler H, et al. (2022). Nonlinear control of transcription through enhancer-promoter interactions. Nature 604, 571–577. 10.1038/s41586-022-04570-y. [PubMed: 35418676]
51. Hnisz D, Abraham BJ, Lee TI, Lau A, Saint-André V, Sigova AA, Hoke HA, and Young RA (2013). Super-enhancers in the control of cell identity and disease. Cell 155, 934–947. 10.1016/j.cell.2013.09.053. [PubMed: 24119843]
52. Gazal S, Weissbrod O, Hormozdiari F, Dey KK, Nasser J, Jagadeesh KA, Weiner DJ, Shi H, Fulco CP, O'Connor LJ, et al. (2022). Combining SNP-to-gene linking strategies to identify disease genes and assess disease omnigenicity. Nat. Genet. 54, 827–836. 10.1038/s41588-022-01087-y. [PubMed: 35668300]
53. Markaki Y, Gan Chong J, Wang Y, Jacobson EC, Luong C, Tan SYX, Jachowicz JW, Strehle M, Maestrini D, Banerjee AK, et al. (2021). Xist nucleates local protein gradients to propagate silencing across the X chromosome. Cell 184, 6174–6192.e32. 10.1016/j.cell.2021.10.022. [PubMed: 34813726]
54. Jachowicz JW, Strehle M, Banerjee AK, Blanco MR, Thai J, and Guttman M (2022). Xist spatially amplifies SHARP/SPEN recruitment to balance chromosome-wide silencing and specificity to the X chromosome. Nat. Struct. Mol. Biol. 29, 239–249. 10.1038/s41594-022-00739-1. [PubMed: 35301492]
55. Schertzer MD, Thulson E, Braceros KCA, Lee DM, Hinkle ER, Murphy RM, Kim SO, Vitucci ECM, and Calabrese JM (2019). A piggyBac-based toolkit for inducible genome editing in mammalian cells. RNA 25, 1047–1058. 10.1261/rna.068932.118. [PubMed: 31101683]
56. Wolff J, Bhardwaj V, Nothjunge S, Richard G, Renschler G, Gilsbach R, Manke T, Backofen R, Ramírez F, and Grüning BA (2018). Galaxy HiCExplorer: a web server for reproducible Hi-C data analysis, quality control and visualization. Nucleic Acids Res. 46, W11–W16. 10.1093/nar/gky504. [PubMed: 29901812]
57. Ramírez F, Bhardwaj V, Arrigoni L, Lam KC, Grüning BA, Villaveces J, Habermann B, Akhtar A, and Manke T (2018). High-resolution TADs reveal DNA sequences underlying genome organization in flies. Nat. Commun. 9, 189. 10.1038/s41467-017-02525-w. [PubMed: 29335486]
58. Dobin A, Davis CA, Schlesinger F, Drenkow J, Zaleski C, Jha S, Batut P, Chaisson M, and Gingeras TR (2013). STAR: ultrafast universal RNA-seq aligner. Bioinformatics 29, 15–21. 10.1093/bioinformatics/bts635. [PubMed: 23104886]
59. Li H, Handsaker B, Wysoker A, Fennell T, Ruan J, Homer N, Marth G, Abecasis G, and Durbin R; 1000 Genome Project Data Processing Subgroup (2009). The Sequence Alignment/Map format and SAMtools. Bioinformatics 25, 2078–2079. 10.1093/bioinformatics/btp352.
60. Quinlan AR, and Hall IM (2010). BEDTools: a flexible suite of utilities for comparing genomic features. Bioinformatics 26, 841–842. 10.1093/bioinformatics/btq033. [PubMed: 20110278]
61. Zhang Y, Liu T, Meyer CA, Eeckhoute J, Johnson DS, Bernstein BE, Nusbaum C, Myers RM, Brown M, Li W, and Liu XS (2008). Model-based analysis of ChIP-Seq (MACS). Genome Biol. 9, R137, gb-2008–9-9-r137 [pii]. 10.1186/gb-2008-9-9-r137. [PubMed: 18798982]
62. Liao Y, Smyth GK, and Shi W (2014). featureCounts: an efficient general purpose program for assigning sequence reads to genomic features. Bioinformatics 30, 923–930. 10.1093/bioinformatics/btt656. [PubMed: 24227677]
63. Wickham H (2016). ggplot2: Elegant Graphics for Data Analysis (Springer-Verlag).
64. Calabrese JM, Starmer J, Schertzer MD, Yee D, and Magnuson T (2015). A survey of imprinted gene expression in mouse trophoblast stem cells. G3 (Bethesda) 5, 751–759. 10.1534/g3.114.016238. [PubMed: 25711832]
65. Quinn J, Kunath T, and Rossant J (2006). Mouse trophoblast stem cells. Methods Mol. Med. 121, 125–148. [PubMed: 16251740]
66. Concordet JP, and Haeussler M (2018). CRISPOR: intuitive guide selection for CRISPR/Cas9 genome editing experiments and screens. Nucleic Acids Res. 46, W242–W245. 10.1093/nar/gky354. [PubMed: 29762716]
67. Davis CP, and West JA (2015). Purification of specific chromatin regions using oligonucleotides: capture hybridization analysis of RNA targets (CHART). Methods Mol. Biol. 1262, 167–182. 10.1007/978-1-4939-2253-6_10. [PubMed: 25555581]

68. Flickinger JL, Gebeyehu G, Buchman G, Haces A, and Rashtchian A (1992). Differential incorporation of biotinylated nucleotides by terminal deoxynucleotidyl transferase. Nucleic Acids Res. 20, 2382. 10.1093/nar/20.9.2382. [PubMed: 1317552]

69. Lee BT, Barber GP, Benet-Pagès A, Casper J, Clawson H, Diekhans M, Fischer C, Gonzalez JN, Hinrichs AS, Lee CM, et al. (2022). The UCSC Genome Browser database: 2022 update. Nucleic Acids Res. 50, D1115–D1122. 10.1093/nar/gkab959. [PubMed: 34718705]

70. Langmead B, and Salzberg SL (2012). Fast gapped-read alignment with Bowtie 2. Nat. Methods 9, 357–359. 10.1038/nmeth.1923. [PubMed: 22388286]

71. Robinson JT, Turner D, Durand NC, Thorvaldsdóttir H, Mesirov JP, and Aiden EL (2018). Juicebox.js Provides a Cloud-Based Visualization System for Hi-C Data. Cell Syst. 6, 256–258.e1. 10.1016/j.cels.2018.01.001. [PubMed: 29428417]

72. Orlando DA, Chen MW, Brown VE, Solanki S, Choi YJ, Olson ER, Fritz CC, Bradner JE, and Guenther MG (2014). Quantitative ChIP-Seq normalization reveals global modulation of the epigenome. Cell Rep. 9, 1163–1170. 10.1016/j.celrep.2014.10.018. [PubMed: 25437568]

73. Justice M, Carico ZM, Stefan HC, and Dowen JM (2020). A WIZ/Cohesin/CTCF Complex Anchors DNA Loops to Define Gene Expression and Cell Identity. Cell Rep. 31, 107503. 10.1016/j.celrep.2020.03.067. [PubMed: 32294452]

74. Frankish A, Diekhans M, Jungreis I, Lagarde J, Loveland JE, Mudge JM, Sisu C, Wright JC, Armstrong J, Barnes I, et al. (2021). Gencode 2021. Nucleic Acids Res. 49, D916–D923. 10.1093/nar/gkaa1087. [PubMed: 33270111]

Highlights

- *Airn*-induced architecture changes coincide with PRC-directed chromatin modifications
- Changes center around regions that form prior contacts with *Airn* locus
- *Airn* lncRNA, PRCs, and PRC-directed modifications are linked by proximity
- Specific DNA regulatory elements can modulate repression by *Airn* in different ways

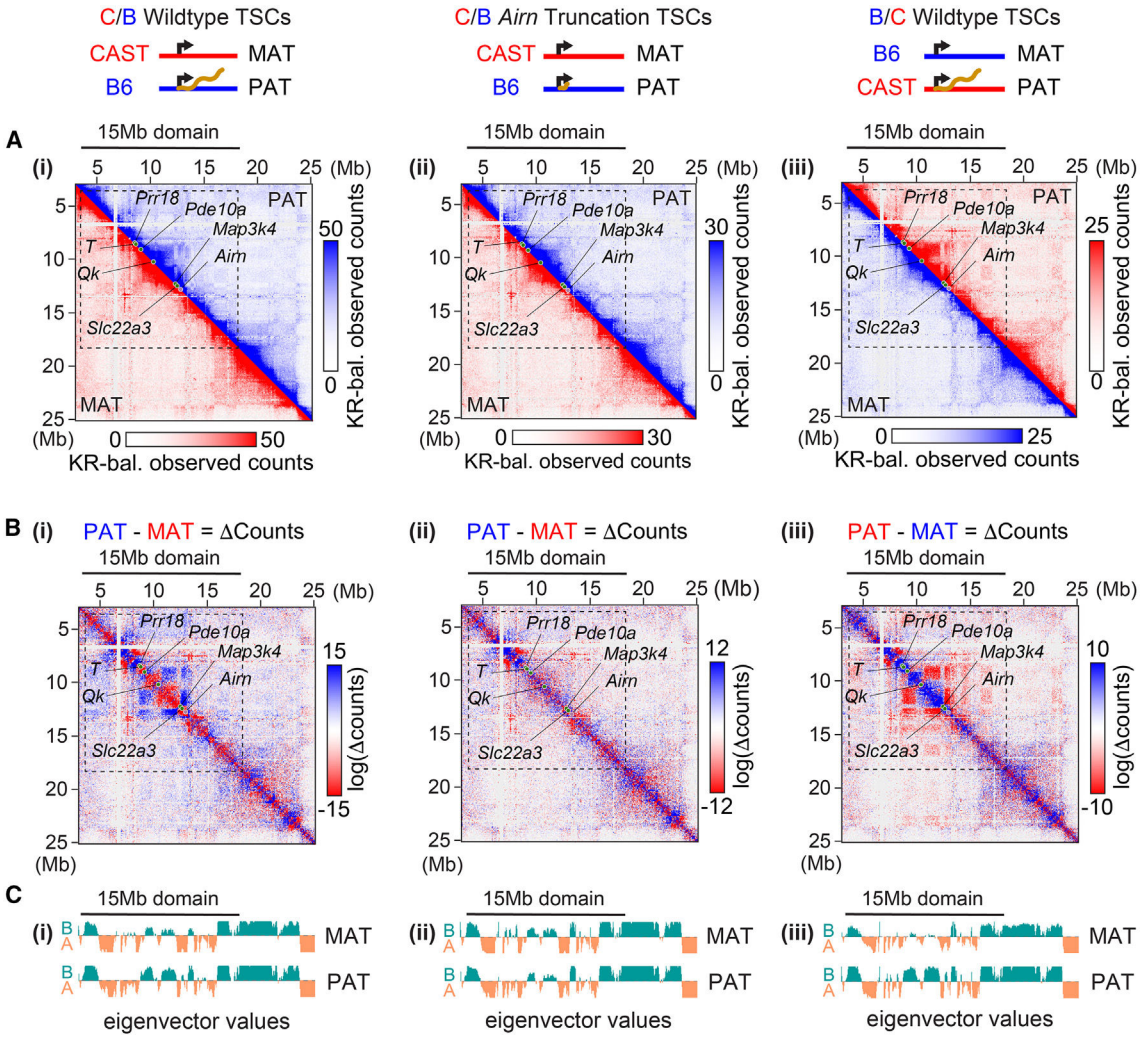

Figure 1. *Airn* expression induces large-scale changes to chromatin architecture

(A) Hi-C contact heatmaps of allelic observed counts in (i) C/B wild-type, (ii) C/B *Airn* truncation, and (iii) B/C wild-type TSCs; n = 2 or 3. Allelic heatmaps are partitioned and at 50-kb resolution.

(B) Subtraction contact heatmaps of log2-transformed (PAT – MAT) observed counts (i–iii) as in (A).

(C) Eigenvectors at 50-kb resolution for "A" and "B" chromosome compartmentalization.[26] In heatmaps: dotted lines, 15-Mb *Airn* target domain; purple circle, *Airn* gene; green circles, other loci of interest. Datasets used are listed in Table S4. KR bal., Knight-Ruiz balanced. See STAR Methods for detailed description of analyses. See also Figure S1.

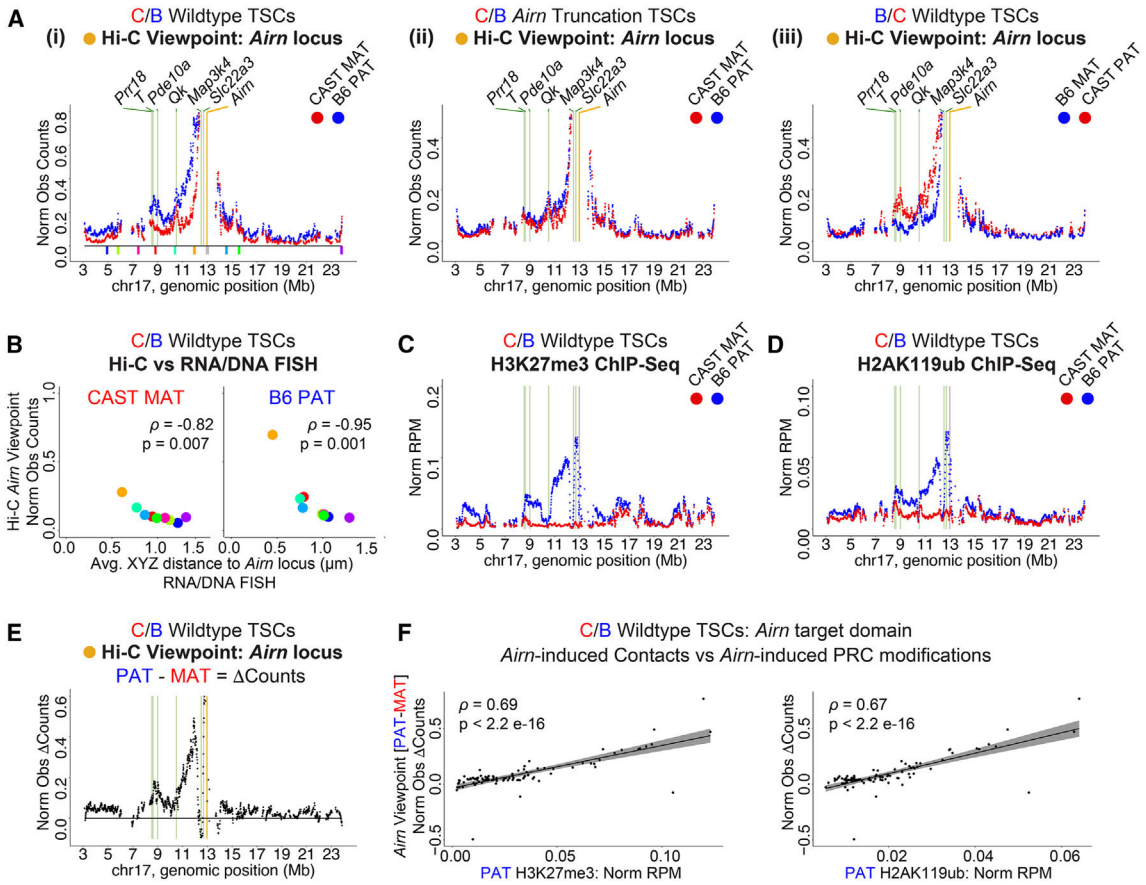

Figure 2. *Airn*-dependent changes in chromatin architecture coincide with the presence of PRC-deposited modifications

(A) Tiling density plots of allelic Hi-C *Airn* viewpoint observed contact counts in (i) C/B wild-type, (ii) C/B *Airn* truncation, and (iii) B/C wild-type TSCs. Colored blocks in (i), and FISH probes analyzed in (B).[14]

(B) Allelic Hi-C *Airn* viewpoint contacts from (Ai) vs. average distance to *Airn* measured by RNA/DNA FISH in C/B wild-type TSCs from Schertzer et al.[14] Spearman's r and p values are shown.

(C and D) Tiling density plots of allelic (C) H3K27me3 ChIP-seq and (D) H2AK119ub ChIP-seq signal in C/B wild-type TSCs. Data are from Schertzer et al.[14] n=4 and 2.

(E) Tiling density plot of allelic *Airn* viewpoint (PAT – MAT) observed counts in C/B wild-type TSCs from (Ai).

(F) Scatterplots of *Airn* viewpoint (PAT – MAT) observed counts vs. (left) H3K27me3 and (right) H2AK119ub. Spearman's r and p values are shown.

In tiling plots: yellow/purple bar, *Airn* viewpoint/gene; green bars, other loci of interest. Datasets used are listed in Table S4. Norm Obs Counts, counts normalized for SNP density; Norm RPM, reads per million total reads normalized for SNP density. See STAR Methods for detailed description of analyses. See also Figure S2.

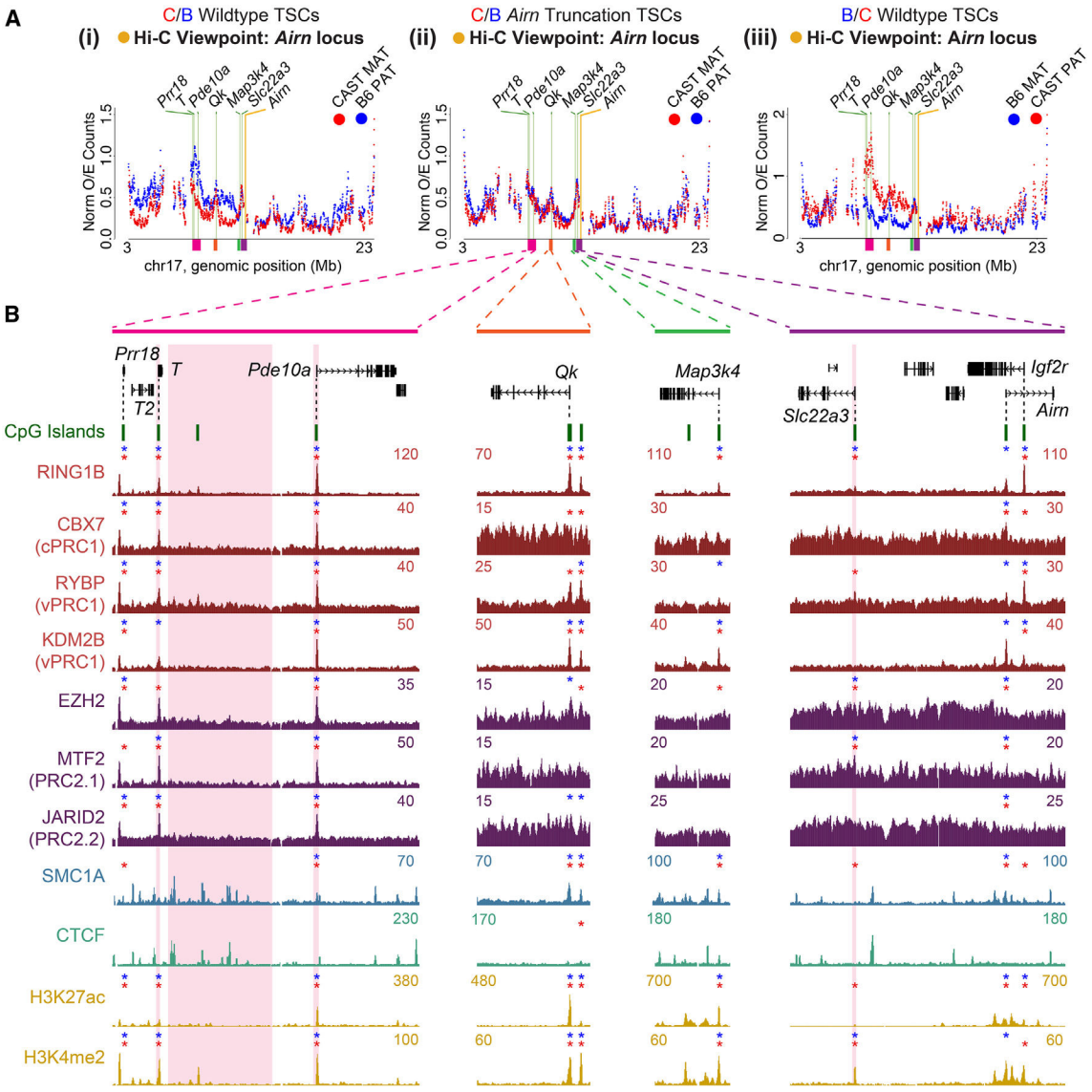

Figure 3. *Airn*-dependent repression centers around regions that form pre-existing contacts with the *Airn* locus and harbor CGIs bound by vPRC1

(A) Tiling density plots of allelic Hi-C *Airn* viewpoint observed-over-expected (O/E) contact counts in (i) C/B wild-type, (ii) C/B *Airn* truncation, and (iii) B/C wild-type TSCs. y axes as in Figure 2. Yellow bar, viewpoint; green bars, other loci of interest.

(B) Genome browser graphics of regions harboring peaks of O/E contact. ChIP-seq tracks, non-allelic read density from C/B wild-type TSCs; n = 2 or 3. Red or blue asterisks, significant enrichment on maternal or paternal alleles, respectively ($p < 0.05$, permutation). Pink rectangles, DNA regions deleted in Figures 5, 6, and 7.

Datasets used are listed in Table S4. See STAR Methods for detailed description of analyses. See also Figure S4 and Table S3.

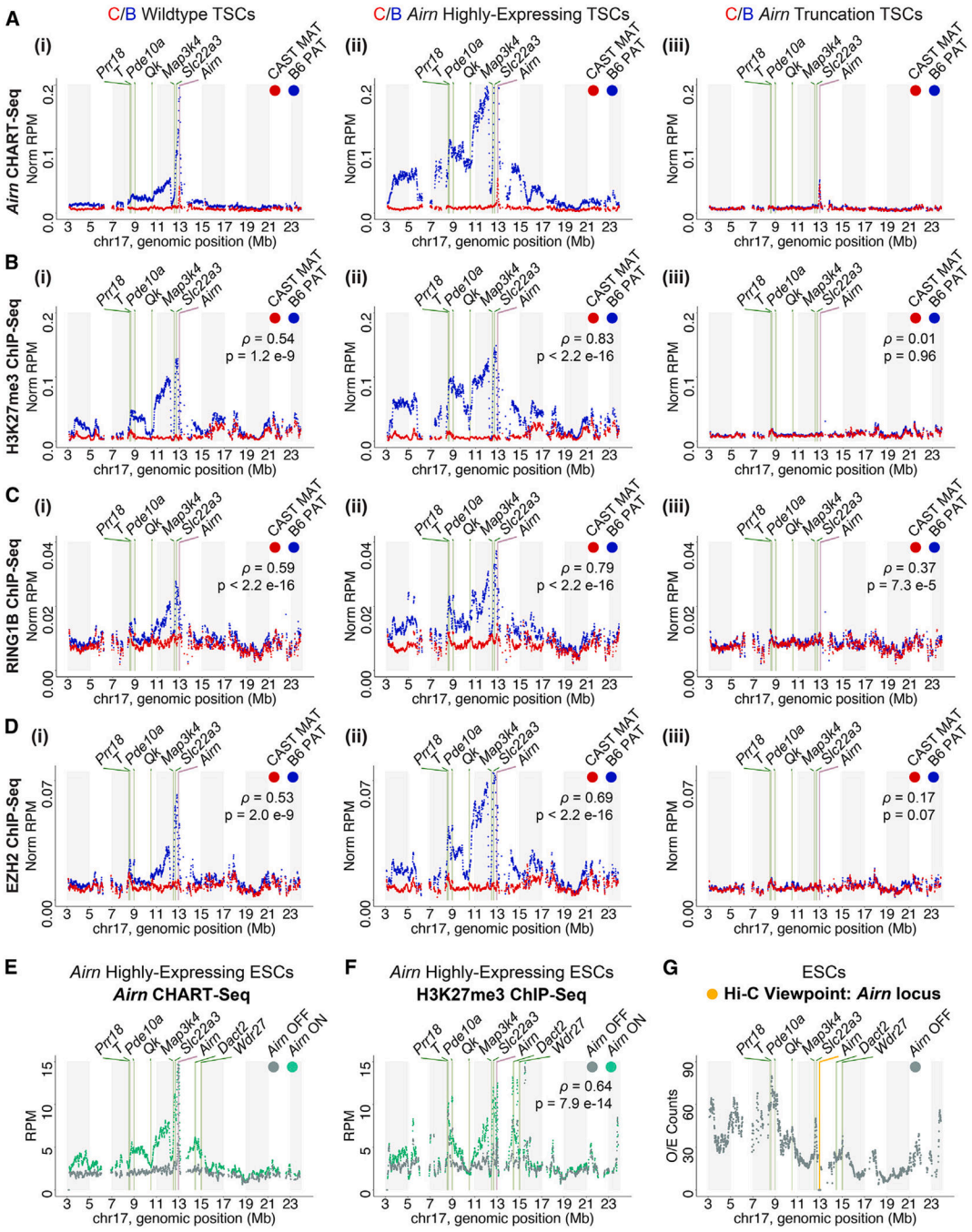

Figure 4. Presence of *Airn* lncRNA on chromatin correlates with presence of PRC1 and PRC2 and centers around pre-existing contacts with the *Airn* locus

(A–D) Tiling density plots of allelic (A) *Airn* CHART-seq, (B) H3K27me3 ChIP-seq, (C) RING1B ChIP-seq, and (D) EZH2 ChIP-seq signal in C/B (i) wild-type, (ii) *Airn* highly expressing (H-E), and (iii) *Airn* truncation TSCs; n = 1 or 2. y axes are as in Figure 2. H3K27me3 and RING1B ChIP-seq data are from Schertzer et al.[14]

(E and F) Tiling density plots of (E) *Airn* CHART-seq and (F) H3K27me3 ChIP-seq signal in untreated (*Airn* OFF) or dox-treated (*Airn* ON) H-E ESCs; n = 1.

(G) Tiling density plot of Hi-C *Airn* viewpoint O/E counts in ESCs.[42] Yellow/purple bar, *Airn* viewpoint/gene; green bars, other loci of interest.

Datasets used are listed in Table S4. See STAR Methods for detailed description of analyses. See also Figures S2 and S5.

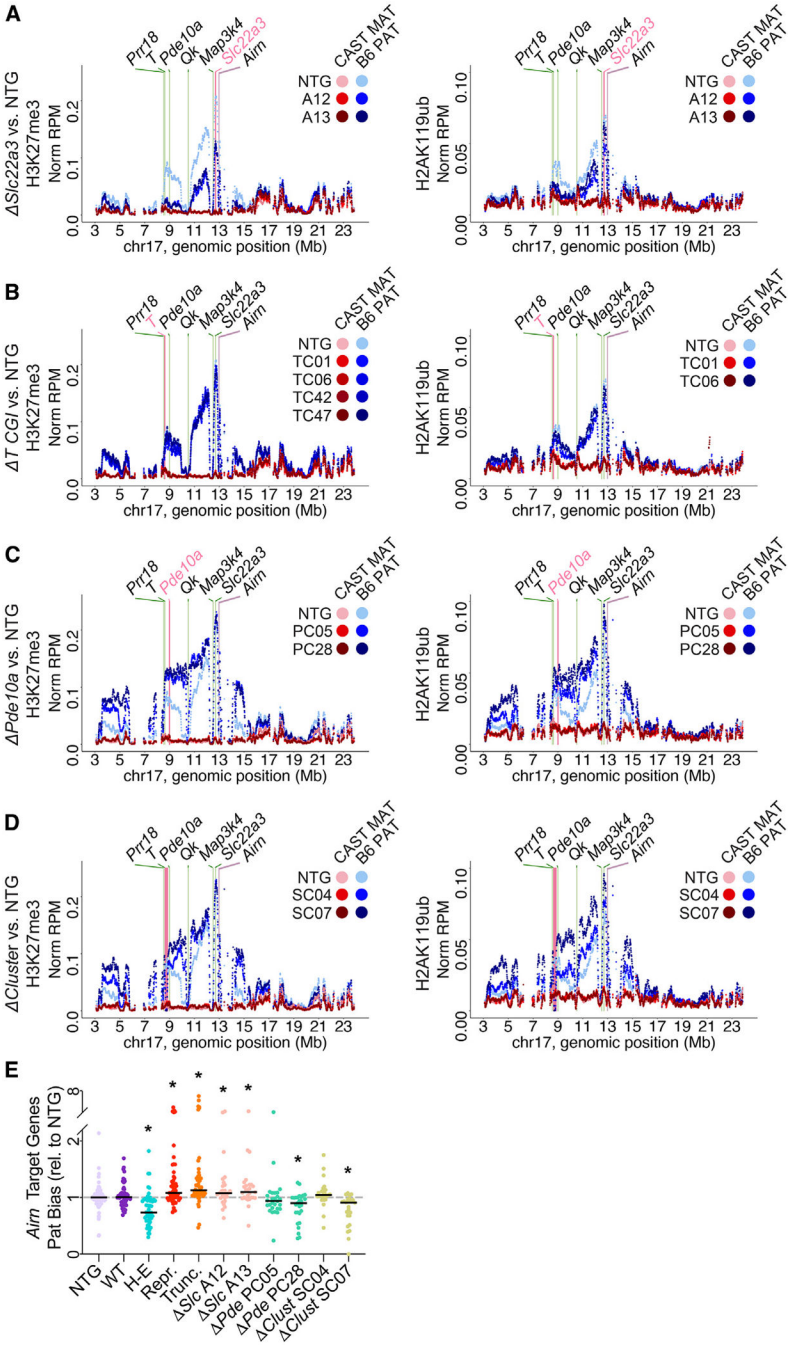

Figure 5. DNA regulatory element deletions alter levels of PRC-directed modifications and gene repression throughout the *Airn* target domain

(A–D) Tiling density plots of allelic (left) H3K27me3 and (right) H2AK119ub ChIP-seq signal in C/B (A) Δ*Slc22a3*, (B) Δ*T*, (C) Δ*Pde10a*, and (D) Δ*Cluster* TSCs; n = 1 per clonal line. y axes are as in Figure 2. Data from NTG clones were averaged; n = 4.

(E) Paternal expression of the 27 *Airn* target genes across genotypes relative to NTG; n = 1, 2, or 4. Asterisks, significant changes relative to NTG ($p < 0.05$, Welch two-sample t test).

In tiling plots: purple bar, *Airn* gene; green bars, other loci of interest; pink bars, DNA regions deleted. Datasets used are listed in Table S4. See STAR Methods for detailed description of analyses. See also Figure S6 and Table S2.

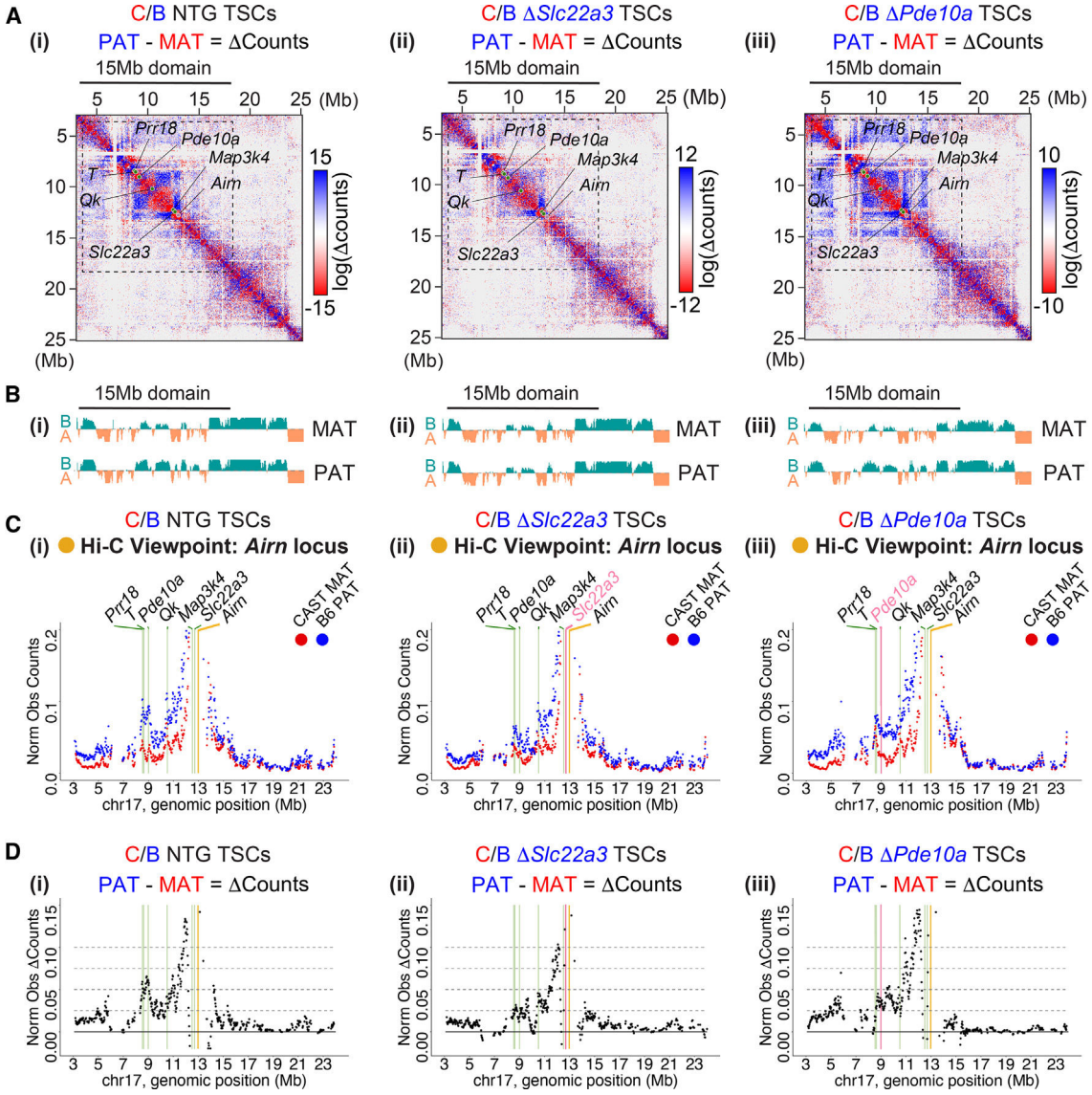

Figure 6. Changes in DNA contacts with *Airn* mirror changes in PRC activity caused by regulatory element deletion

(A) Hi-C subtraction contact heatmaps of log2-transformed (PAT – MAT) observed counts in C/B (i) NTG, (ii) Δ*Slc22a3*, and (iii) Δ*Pde10a* TSCs; n = 2.

(B) Eigenvectors at 50-kb resolution for “A” and “B” chromosome compartmentalization (i–iii) as in (A).

(C) Tiling density plots of allelic *Airn* viewpoint observed contact counts (i–iii) as in (A). y axes as in Figure 2.

(D) Tiling density plots of allelic *Airn* viewpoint (PAT – MAT) observed counts (i–iii) as in (A).

In heatmaps: dotted lines, 15-Mb *Airn* target domain; purple circles, *Airn* gene; green circles, other loci of interest. In tiling plots: yellow bar, *Airn* locus viewpoint; green bars, other loci of interest; pink bar, DNA region deleted. Datasets used are listed in Table S4. See STAR Methods for detailed description of analyses. See also Figure S7.

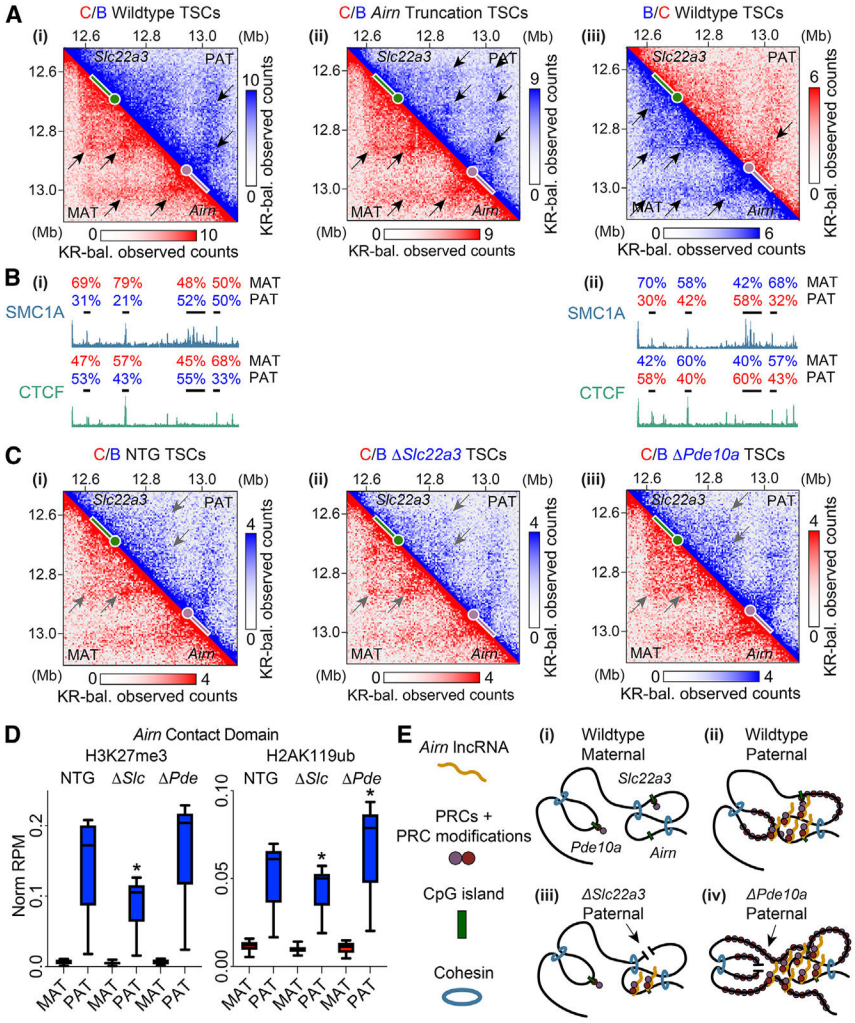

Figure 7. *Airn* expression is coincident with dissolution of DNA loops encasing *Slc22a3* and a local increase in PRC-directed modifications

(A) Allelic Hi-C contact heatmaps of the *Airn* contact domain at 5-kb resolution in (i) C/B wild-type, (ii) C/B *Airn* truncation, and (iii) B/C wild-type TSCs. Black arrows, SIP-called DNA loops.

(B) SMC1A/Cohesin and CTCF ChIP-seq. Percent parental biases at loops (i and ii) as in (A).

(C) Allelic contact heatmaps of *Airn* contact domain at 5-kb resolution in C/B (i) NTG, (ii) Δ*Slc22a3*, and (iii) Δ*Pde10a* TSCs. Gray arrows, DNA loops of interest from (A). In heatmaps: circles, 5′ end of genes/CGIs; rectangles, gene bodies; purple, *Airn* gene; green, *Slc22a3* gene.

(D) Boxplots of average allelic (left) H3K27me3 and (right) H2AK119 ChIP-seq signal over *Airn* contact domain in NTG, Δ*Slc22a3*, and Δ*Pde10a* TSCs; n = 2. Asterisks, significant changes relative to NTG ($p < 0.05$, Welch two-sample t test). Error bars, data points outside the interquartile range.

(E) Model: DNA regulatory elements modulate frequency of contact with and repression by *Airn*. (i) On maternal allele, pre-existing contacts with *Airn* locus render certain regions

more susceptible torepression than others. (ii) On paternal allele, PRCs and PRC-deposited modifications to chromatin increase contacts with *Airn* locus, which in turn increase intensity of long-distance repression. (iii) Loss of *Slc22a3* CGI attenuates repression by reducing local PRC recruitment and contact with distal regions. (iv) Loss of *Pde10a* CGI increases frequency with which surrounding regions contact *Airn*.

Datasets used are listed in Table S4. See STAR Methods for detailed description of analyses.

KEY RESOURCES TABLE

REAGENT or RESOURCE	SOURCE	IDENTIFIER
Antibodies		
H3K27me3	Cell Signaling	Cat#9733; RRID: AB_2616029
H2AK119ub	Cell Signaling	Cat#8240; RRID: AB_10891618
RING1B	Cell Signaling	Cat#5694; RRID: AB_10705604
CBX7	Abcam	Cat#ab21873; RRID: AB_726005
DEDAF (RYBP)	Millipore	Cat#AB3637; RRID: AB_11213333
JHDM1B (KDM2B)	Millipore	Cat#09–864; RRID: AB_10806072
EZH2	Cell Signaling	Cat#5246; RRID: AB_10694683
MTF2	Proteintech	Cat#16208–1-AP; RRID: AB_2147370
JARID2	Cell Signaling	Cat#13594; RRID: AB_2798269
Chemicals, peptides, and recombinant proteins		
Heparin Sodium Salt	Sigma-Aldrich	Cat#H3149
FGF4 Recombinant Human Protein	Gibco	Cat#PHG0154
RPMI 1640	Gibco	Cat#11875093
DMEM, high glucose, sodium pyruvate	Gibco	Cat#11995073
Fetal Bovine Serum, qualified	Gibco	Cat#26140079
Penicillin-Streptomycin	Gibco	Cat#15140122
L-glutamine	Gibco	Cat#25030081
MEM Non-essential Amino Acids	Gibco	Cat#11140050
Sodium Pyruvate	Gibco	Cat#11360070
β-mercaptoethanol	Sigma-Aldrich	Cat#63689
LIF	Lif-1Cα/COS-conditioned ESC media	N/A
Trypsin-EDTA, phenol red	Gibco	Cat#2520072
LipoFectamine 3000	Invitrogen	Cat#L3000015
10X Phosphate-Buffered Saline (PBS)	Corning	Cat#46–013-CM
Pierce 16% Formaldehyde	Thermo Scientific	Cat#28906
37% Formaldehyde	Fisher Scientific	Cat#BP531–500
TRIzol Reagent	Invitrogen	Cat#15596026
Chloroform	Fisher Scientific	Cat#BP1145–1
25:24:1 Phenol:Chloroform:Isoamyl Alcohol	Sigma-Aldrich	Cat#6805
Protein A/G PLUS Agarose Beads	Santa Cruz Biotechnology	Cat#sc-2003
AMPure XP Beads	Beckman Coulter	Cat#A63880
Dynabeads M-280 Streptavidin	Invitrogen	Cat#11205D
Dynabeads MyOne Streptavidin C1	Invitrogen	Cat#65002
Ribonuclease A (RNase A) from bovine pancreas	Sigma-Aldrich	Cat#R4642
Proteinase K Solution	Bioline	Cat#BIO-37084
Proteinase K (Fungal)	Invitrogen	Cat#25530015
Linear Acrylamide	Invitrogen	Cat#AM9520

REAGENT or RESOURCE	SOURCE	IDENTIFIER
Choice Taq	Denville	Cat#CB4050–2
Phusion High-Fidelity DNA Polymerase	New England Biolabs	Cat#M0530S
Biotin-16-dUTP	Roche	Cat#11093070910
Terminal Deoxynucleotidyl Transferase	Thermo Scientific	Cat#EP0161
Klenow Fragment (3'->5' exo)	New England Biolabs	Cat#M0212S
dATP Solution	Invitrogen	Cat#10–216-018
Critical commercial assays		
Neon Transfection System 100μL Kit	Invitrogen	Cat#MPK10025
QIAquick Nucleotide Removal Kit	Qiagen	Cat#28304
Zymo Research RNA Clean & Concentrator	Zymo Research Kit	Cat#50–125-1669
Arima-HiC + Kit	Arima Genomics	Cat#A510008
KAPA RNA HyperPrep with RiboErase	Roche/KAPA Biosystems (HMR)	Cat#KK8561
NEBNext End Repair Module	New England Biolabs	Cat#E6050S
Quick Ligation Kit	New England Biolabs	Cat#M2200S
NEBNext High-Fidelity 2X PCR Master Mix	New England Biolabs	Cat#M0541S
High-Capacity cDNA Reverse Transcription Kit	Applied Biosystems	Cat#4368814
iTaq Universal SYBR Green Supermix	Bio-Rad	Cat#1725125
PureLink HiPure Plasmid Midiprep Kit	Invitrogen	Cat#K2100004
Deposited data		
Raw and analyzed sequencing data	This study; see Table S4	GEO: GSE217262
Mouse reference genome NCBI build 37, NCBI37/mm9	Genome Reference Consortium	https://www.ncbi.nlm.nih.gov/grc/mouse
Variant sequence data	Sanger Institute	https://www.sanger.ac.uk/data/mouse-genomes-project/
Experimental models: Cell lines		
Mouse: C/B and B/C trophoblast stem cells	This study	N/A
Mouse: E14 embryonic stem cells	This study	N/A
Mouse: DR4 embryonic fibroblast cells	ATCC	Cat#SCRC-1045
Oligonucleotides		
CRISPR-Cas9 sgRNAs, see Table S5	This study	N/A
Genotyping PCR primers, see Table S5	This study	N/A
qPCR primers, see Table S5	This study	N/A
Recombinant DNA		
PB_tre_dCas9_VP160 vector	Schertzer et al.[55]	Cat#126031;https://doi.org/10.1261/rna.068932.118
PB_tre_Cas9 vector	Schertzer et al.[55]	Cat#126029;https://doi.org/10.1261/rna.068932.118
PB_rtTA_BsmBI vector Schertzer et al.[55]	Schertzer et al.[55]	Cat#126028;https://doi.org/10.1261/rna.068932.118

REAGENT or RESOURCE	SOURCE	IDENTIFIER
pUC19-piggyBac transposase	Schertzer et al.[55]	https://doi.org/10.1261/rna.068932.118
Software and algorithms		
Custom Scripts	This study	https://github.com/aki-kb/calabrese_lab/tree/main/braceros_airn_2023;https://doi.org/10.5281/zenodo.7988247
Juicer/Juicebox (v1.5.6)	Durand et al.[27,28]	https://github.com/aidenlab/juicer;https://github.com/aidenlab/Juicebox
Juicer Tools (v1.9.9)	Durand et al.[27]	https://github.com/aidenlab/juicer
HiCExplorer (v3.7.2)	Wolff et al.,[56] Ramirez et al.[57]	https://hicexplorer.readthedocs.io/en/latest
Bowtie2 (v2.4.5)	Langmead and Salzberg[58]	http://bowtie-bio.sourceforge.net/bowtie2/index.shtml
STAR (v2.7.9a)	Dobin et al.[58]	https://github.com/alexdobin/STAR
Samtools (v1.16)	Li et al.59	https://github.com/samtools/samtools
Bedtools (v2.30)	Quinlan and Hall60	https://bedtools.readthedocs.io/en/latest
Significant Peak Interaction (SIP; v1.5)	Rowley et al.[43]	https://github.com/PouletAxel/SIP
MACS2 (v2.1.2)	Zhang et al.[61]	https://github.com/taoliu/MACS
Subread: featureCounts (v1.6.3)	Liao et al.[62]	http://subread.sourceforge.net
RStudio (v4.2.0)	N/A	https://posit.co/products/open-source/rstudio
ggplot2, ggpubr (v3.3.5)	Wickham[63]	https://ggplot2.tidyverse.org
GraphPad Prism (v9.4.1)	N/A	https://www.graphpad.com
Other		
Vibra-Cell™ VCX 130 Sonicator & 6mm Probe	Sonics	Cat#H-1002–2
Bioruptor® Plus sonication device	Diagenode	Cat#B01020001